A minimal-length approach unifies rigidity in underconstrained materials

Merkel, Matthias; Baumgarten, Karsten; Tighe, Brian P.; Manning, M. Lisa

DOI
10.1073/pnas.1815436116

Publication date
2019

Document Version
Accepted author manuscript

Published in
Proceedings of the National Academy of Sciences of the United States of America

A minimal-length approach unifies rigidity in under-constrained materials

Matthias Merkel[a,b,1], **Karsten Baumgarten**[c], **Brian P. Tighe**[c], **and M. Lisa Manning**[a]

[a]Department of Physics, Syracuse University, Syracuse, New York 13244, USA; [b]Centre de Physique Théorique (CPT), Turing Center for Living Systems, Aix Marseille Univ, Université de Toulon, CNRS, 13009 Marseille, France; [c]Delft University of Technology, Process & Energy Laboratory, Leeghwaterstraat 39, 2628 CB Delft, The Netherlands

This manuscript was compiled on May 6, 2019

We present a novel approach to understand geometric-incompatibility-induced rigidity in under-constrained materials, including sub-isostatic 2D spring networks and 2D and 3D vertex models for dense biological tissues. We show that in all these models a geometric criterion, represented by a minimal length $\bar{\ell}_{\min}$, determines the onset of prestresses and rigidity. This allows us to predict not only the correct scalings for the elastic material properties, but also the precise *magnitudes* for bulk modulus and shear modulus discontinuities at the rigidity transition as well as the magnitude of the Poynting effect. We also predict from first principles that the ratio of the excess shear modulus to the shear stress should be inversely proportional to the critical strain with a prefactor of three, and propose that this factor of three is a general hallmark of geometrically induced rigidity in under-constrained materials and could be used to distinguish this effect from nonlinear mechanics of single components in experiments. Lastly, our results may lay important foundations for ways to estimate $\bar{\ell}_{\min}$ from measurements of local geometric structure, and thus help develop methods to characterize large-scale mechanical properties from imaging data.

biopolymer networks | vertex model | constraint counting | under-constrained | minimal length | rigidity | strain stiffening

A material's rigidity is intimately related to its geometry. In materials that crystallize, rigidity occurs when the constituent parts organize on a lattice. In contrast, granular systems can rigidify while remaining disordered, and arguments developed by Maxwell (1) accurately predict that the material rigidifies at an isostatic point where the number of constraints on particle motion equal the number of degrees of freedom.

Further work by Calladine (2) highlighted the important role of states of self stress, demonstrating that an index theorem relates rigidity to the total number of constraints, degrees of freedom, and self stresses. Recent work has extended these ideas in both ordered and disordered systems to design materials with geometries that permit topologically protected floppy modes (3–5).

A third way to create rigidity is through geometric incompatibility, which we illustrate by a guitar string. Before it is tightened, the floppy string is under-constrained, with fewer constraints than degrees of freedom, and there are many ways to deform the string at no energetic cost. As the distance between the two ends is increased above the rest length of the string, this geometric incompatibility together with the accompanying creation of a self-stress rigidifies the system (3, 6). Any deformation will be associated with an energetic cost, leading to finite vibrational frequencies. This same mechanism has been proposed to be important for the elasticity of rubbers and gels (6) as well as biological cells (7).

In particular, it has been shown to rigidify under-constrained, disordered fiber networks under applied strain, with applications in biopolymer networks (8–22). Just as with the guitar string, rigidity arises when the size and shape of the box introduce external constraints that are incompatible with the local segments of the network attaining their desired rest lengths. For example, when applying external shear, fiber networks strongly rigidify at some critical shear strain γ^* (9, 14, 16, 18–20, 22, 23), although it remains controversial whether the onset of rigidity is continuous (14, 15, 20, 24) or discontinuous (18) in the limit without fiber bending rigidity. Similarly, fiber networks can also be rigidified by isotropic dilation (10), and the interaction between isotropic and shear elasticity in these systems is characterized an anomalous negative Poynting effect (19, 21, 25–27), i.e. the development of a tensile normal stress in response to externally applied simple shear. However, it has as yet remained unclear how all of these observations and their critical scaling behavior (9, 16, 18, 20, 28) are quantitatively connected to the underlying geometric structure of the network. Moreover, while previous works have remarked that several features of stiffening in fiber networks are surprisingly independent of model details (13), it has remained elusive whether there are generic underlying mechanisms.

Rigidity transitions have also been identified in dense biological tissues (29–33). In particular, vertex or Voronoi models that describe tissues as a tessellation of space into polygons or polyhedra exhibit rigidity transitions (34–49), which share

Significance Statement

What do a guitar string and a balloon have in common? They are both floppy unless rigidified by geometrically induced prestresses. The same kind of rigidity transition in under-constrained materials has more recently been discussed in the context of disordered biopolymer networks and models for biological tissues. Here, we propose a general approach to quantitatively describe such transitions. Based on a minimal length function, which scales linearly with intrinsic fluctuations in the system and quadratically with shear strain, we make concrete predictions about the elastic response of these materials, which we verify numerically and which are consistent with previous experiments. Finally, our approach may help develop methods that connect macroscopic elastic properties of disordered materials to their microscopic structure.

M.M., B.P.T., and M.L.M. designed the research, M.M. performed the research and analyzed the data, K.B. provided important simulation data, M.M., B.P.T., and M.L.M. wrote the paper.

The authors declare no conflict of interest.

[1]To whom correspondence should be addressed. E-mail: mmerkel@syr.edu

Table 1. Models discussed in this article. For the spring networks, the values indicated apply to a system size of $2N/z = 1024$ nodes, and for all cellular models values apply to a system size of $N = 512$ cells. For each model, we indicate the respective dimension d of the "length springs" and the spatial dimension D, as well as the numbers of degrees of freedom (dof) as well as constraints (i.e. length + area springs). The provided values for transition point ℓ_0^* and geometric coefficients a_ℓ, a_a, and b are average values extracted from simulations exploring the rigid regime near the transition point. For the cellular models, they are indicated together with their standard deviations across different random realizations. For the 2D spring networks, the indicated numbers and their uncertainty corresponds to the respective fit of the average values with fixed exponent of Δz. Differences to earlier publications (37, 44, 46) result from differences in sampling due to a different energy minimization protocol used here (Supplemental Information, section IV).

Model	"Area" rigidity	Dimension d	D	Number of dof	constraints	Transition point ℓ_0^*	Coefficients a_ℓ	a_a	b
2D spring network	–	1	2	$4N/z$	N	(1.506 ± 0.004) $-(0.378 \pm 0.009)\Delta z$	$(1.33 \pm 0.06)/\Delta z^{1/2}$	–	$(0.7 \pm 0.1)/\Delta z$
2D vertex model	$k_A = 0$	1	2	$4N$	N	3.87 ± 0.01	0.30 ± 0.01	–	0.48 ± 0.02
2D vertex model	$k_A > 0$	1	2	$4N$	$2N$	3.92 ± 0.01	1.7 ± 0.4	3.3 ± 0.7	0.6 ± 0.2
2D Voronoi model	$k_A = 0$	1	2	$2N$	N	3.82 ± 0.01	0.64 ± 0.03	–	0.68 ± 0.03
3D Voronoi model	$k_V = 0$	2	3	$3N$	N	5.375 ± 0.003	0.25 ± 0.01	–	0.61 ± 0.02
3D Voronoi model	$k_V > 0$	2	3	$3N$	$2N$	5.406 ± 0.004	2.0 ± 0.1	6.6 ± 0.4	1.1 ± 0.1

similarities with both particle-based models, where the transition is driven by changes to connectivity (48), and fiber (or spring) networks, which can be rigidified by strain. Therefore, an open question is how both connectivity and strain can interact to rigidify materials (22).

Very recently, some of us showed that the 3D Voronoi model exhibits a rigidity transition driven by geometric incompatibility (46), similar to fiber networks. This has also been demonstrated for the 2D vertex model, using a continuum elasticity approach based on a local reference metric (42). For the case of the 3D Voronoi model, we found that there was a special relationship between properties of the network geometry and the location of the rigidity transition, largely independent of the realization of the disorder (46).

Here, we show that such a relationship between rigidity and geometric structure is generic to a broad class of under-constrained materials, including spring networks and vertex/Voronoi models in different dimensions (Table 1, Figure 1). We first demonstrate that all these models display the same generic behavior in response to isotropic dilation. Understanding key geometric structural properties of these systems allows us to predict the precise values of a discontinuity in the bulk modulus at the transition point. We then extend our approach to include shear deformations, which allows us to analytically predict a discontinuity in the shear modulus at the onset of rigidity. Moreover, we can make precise quantitative predictions of the values of critical shear strain γ^*, scaling behavior of the shear modulus beyond γ^*, Poynting effect, and several related critical exponents. In each case, we numerically demonstrate the validity of our approach for the case of spring networks.

We also compare our predictions to previously published experimental data, and highlight some new predictions, including a prefactor of three that we expect to find generically in a scaling collapse of the shear modulus, shear stress, and critical strain.

We achieve these results by connecting macroscopic mechanical network properties to underlying geometric properties. In the case of the guitar string, the string first becomes taut when the distance between the two ends attains a critical value ℓ_0^* equal to the intrinsic length of the string, so that the boundary conditions for the string are geometrically incompatible with the intrinsic geometry of the string. As the string is stretched, one can predict its pitch (or equivalently the effective elastic modulus) by quantifying the actual length of the string ℓ relative to its intrinsic length. While this is straightforward in the one-dimensional geometry of a string, we are interested in understanding whether a similar geometric principle, based on the average length of a spring $\bar{\ell}$ governs the behavior near the onset of rigidity in disordered networks in 2D and 3D.

Here, we formulate a geometric compatibility criterion in terms of the constrained minimization of the average spring length $\bar{\ell}_{\min}$ in a disordered network. Just as for the guitar string, this length $\bar{\ell}_{\min}$ attains a critical value ℓ_0^* at the onset of rigidity. As the system is strained beyond the rigidity transition, we demonstrate analytically and numerically that the geometry constrains $\bar{\ell}_{\min}$ to vary in a simple way with two observables: fluctuations of spring lengths σ_l, and shear strain γ. Because $\bar{\ell}_{\min}$ is minimized over the whole network, it is a collective geometric property of the network.

Just as with the guitar string, the description of the geometry given by $\bar{\ell}_{\min}$ then allows us to calculate many features of the elastic response, including the bulk and shear moduli. This in turn provides a general basis to analytically understand the strain-stiffening responses of under-constrained materials to both isotropic and anisotropic deformation within a common framework. Even though $\bar{\ell}_{\min}$ describes collective geometric effects, our work may also provide an important foundation to understand macroscopic mechanical properties from *local* geometric structure.

Models

Here we focus on four classes of models, which include 2D sub-isostatic random spring networks without bending rigidity (9, 50–54) and three models for biological tissues: the 2D vertex model (34, 37), the 2D Voronoi model (38, 44), and the 3D Voronoi model (46) (Table 1).

2D spring networks consist of nodes that are connected by in total N springs, where the average number of springs connected to a node is the coordination number z. We create networks with a defined value for z by translating jammed configurations of bidisperse disks into spring networks and then randomly pruning springs until the desired coordination number z is reached (9, 27). We use harmonic springs, such

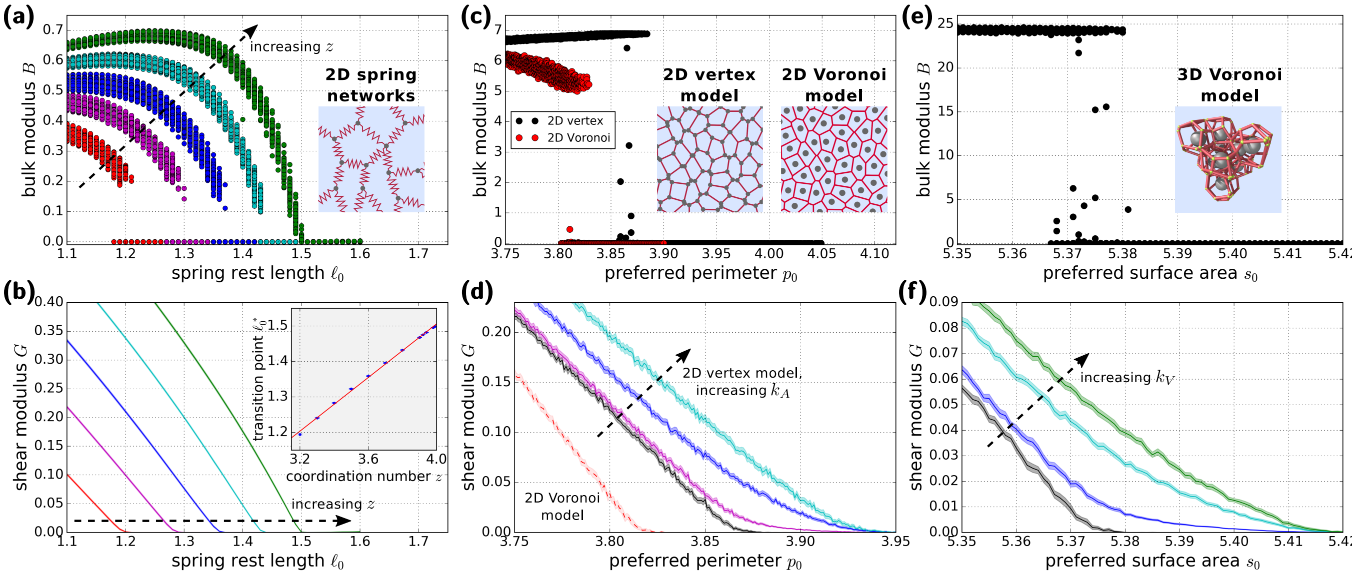

Fig. 1. Comparison of the rigidity transition across the different models: (a,b) 2D spring network (coordination numbers $z = 3.2, 3.4, 3.6, 3.8, 3.99$), (c,d) 2D Voronoi model (with $k_A = 0$) and 2D vertex model (with $k_A = 0$ in panel c and $k_A = 0, 0.1, 1, 10$ in panel d), (e,f) 3D Voronoi model (with $k_V = 0$ in panel e and $k_V = 0, 1, 10, 100$ in panel f). In all models, the transition is discontinuous in the bulk modulus (panels a,c,e) and continuous in the shear modulus (panels b,d,f). (b inset) For 2D spring networks, the value of the transition point ℓ_0^* (quantified using the bisection protocol detailed in section IVB of the Supplemental Information) increases with the coordination number z. This relation is approximately linear in the vicinity of the isostatic point $z_c \equiv 4$. Blue dots are simulation data and the red line shows a linear fit with $\ell_0^* = (1.506 \pm 0.004) - (0.378 \pm 0.009)\Delta z$ with $\Delta z = z_c - z$. Close to the transition point in panels c,e, data points are scattered between zero and a maximal value. This scattering is due to insufficient energy minimization in these cases. In panels b, d, and f, shaded regions indicate the standard error of the mean.

that the total mechanical energy of the system is:

$$e_{s2D} = \sum_i (l_i - l_{0i})^2. \tag{1}$$

Here, the sum is over all springs i with length l_i and rest length l_{0i}, which are generally different for different springs. For convenience, we re-express Eq. (1) in terms of a mean spring rest length $\ell_0 = [(\sum_i l_{0i}^2)/N]^{1/2}$, which we use as a control parameter acting as a common scaling factor for all spring rest lengths. This allows us to rewrite the energy as:

$$e_{s2D} = \sum_i w_i(\ell_i - \ell_0)^2 \tag{2}$$

with rescaled spring lengths $\ell_i = \ell_0 l_i / l_{0i}$ and weights $w_i = (l_{0i}/\ell_0)^2$, such that $\sum_i w_i = N$ (for details, see Supplemental Information, section IA). In simple constraint counting arguments, each spring is treated as one constraint, and here we are interested in *sub-isostatic* (i.e under-constrained, also called *hypostatic*) networks with $z < z_c \equiv 4$.

The tissue models describe biological tissues as polygonal (2D) or polyhedral (3D) tilings of space. For the Voronoi models, these tilings are Voronoi tessellations and the degrees of freedom are the Voronoi centers of the cells. In contrast, in the 2D vertex model, the degrees of freedom are the positions of the vertices (i.e. the polygon corners). Forces between the cells are described by an effective energy functional. For the 2D models, the (dimensionless) energy functional is:

$$e_{c2D} = \sum_i \left[(p_i - p_0)^2 + k_A (a_i - 1)^2 \right]. \tag{3}$$

Here, the sum is over all N cells i with perimeter p_i and area a_i. There are two parameters in this model: the preferred perimeter p_0 and the relative area elasticity k_A. For the 3D Voronoi model, the energy is defined analogously:

$$e_{c3D} = \sum_i \left[(s_i - s_0)^2 + k_V (v_i - 1)^2 \right]. \tag{4}$$

The sum is again over all N cells i of the configuration, with cell surface area s_i and volume v_i, and the two parameters of the model are preferred surface area s_0 and relative volume elasticity k_V.

All four of these models are under-constrained based on simple constraint counting, as is apparent from the respective numbers of degrees of freedom and constraints listed in Table 1. We stress that Calladine's constraint counting derivation (2, 3) also applies to many-particle, non-central-force interactions.

Throughout this article, we will often discuss all four models at once. Thus, when generally talking about "elements", we refer to springs in the spring networks and cells in the tissue models. Similarly, when talking about "lengths ℓ" (of dimension d), we refer to spring lengths ℓ in the spring networks, cell perimeters p in the 2D tissue models, and cell surface areas s in the 3D tissue model (Table 1). Finally, when talking about "areas a" (of dimension D), we refer to cell areas a in the 2D tissue models as well as cell volumes v in the 3D tissue model.

Here we study the behavior of local energy minima of all four models under periodic boundary conditions with fixed dimensionless system size N, i.e. the model is non-dimensionalized such that the average area per element is one (41, 44, 46). Under these conditions, a rigidity transition exists in all models even without area rigidity. In particular, for the 2D vertex and 3D Voronoi models, we discuss the special case $k_A = 0$ separately (Table 1). Moreover, the athermal 2D Voronoi model does not exhibit a rigidity transition for $k_A > 0$ (44), and thus we will only discuss the case $k_A = 0$ for this model.

Results

A. Rigidity is created by geometric incompatibility corresponding to a minimal length criterion. We start by comparing the rigidity transitions in the four different models using Figure 1, where we plot both the differential bulk modulus B and the differential shear modulus G versus the preferred length ℓ_0. In this first part, we use for all models the preferred length ℓ_0 as a control parameter. Note that because ℓ_0 is non-dimensionalized using the number density of elements, changing ℓ_0 corresponds to applying isotropic strain (i.e. a change in volume with no accompanying change in shape). Later, we will additionally include the shear strain γ as a control parameter.

In all models, we find a rigid regime ($B, G > 0$) for preferred lengths below the transition point ℓ_0^*, and a floppy regime ($B = G = 0$) above it, with the transition being discontinuous in the bulk modulus and continuous in the shear modulus. For the spring networks, we find that the transition point ℓ_0^* depends on the coordination number, where close to the isostatic point $z_c \equiv 4$, it scales linearly with the distance $\Delta z = z_c - z$ to isostaticity (Figure 1b inset), as previously similarly discussed in (10). Something similar has also been reported for a 2D vertex model (48).

For the cellular models, we find that the transition point for the case without area rigidity, $k_A = 0$, is generally smaller than in the case with area rigidity, $k_A > 0$ (Figure 1d,f, Table 1). Moreover, our 2D vertex model transition point for $k_A > 0$ is somewhat higher than reported before (37). Here we used a different vertex model implementation than in (37) (Supplemental Information, section IVC), and the location of the transition in vertex models depends somewhat on the energy minimization protocol (44), a feature that is shared with other models for disordered materials (55). Also, in Figure 1d,f the *averaged* shear modulus always becomes zero at a higher value than the respective average transition point listed in Table 1. This is due to the distribution of transition points having a finite width (see also finite width of ℓ_0 regions with both zero and nonzero bulk moduli in panels c and e).

We find that in all these models, the mechanism creating the transition is the same: rigidity is created by geometric incompatibility, which is indicated by the existence of prestresses. We have already shown this for the 3D Voronoi model (46) and the 2D Voronoi model with $k_A = 0$ (44), while others have shown this for the *ordered* 2D vertex model (42). Furthermore, our data confirms that this is the case for the 2D spring networks and the $k_A = 0$ cases of both (disordered) 2D vertex and 3D Voronoi models (Supplemental Information, section IIA).

We find something similar for the disordered 2D vertex model for $k_A > 0$. Although there are special cases where prestresses appear also in the floppy regime (Supplemental Information, section IIA), to simplify our discussion here, we only consider configurations without such typically localized prestresses.

We observe that in all of these models, a geometric criterion, which we describe in terms of a minimal average length $\bar{\ell}_{\min}$, determines the onset of prestresses. For example, we can exactly transform the spring network energy Eq. (2) into (Supplemental Information, section IA):

$$e_{s2D} = N\Big[(\bar{\ell} - \ell_0)^2 + \sigma_\ell^2\Big]. \quad [5]$$

Here, $\bar{\ell} = (\sum_i w_i \ell_i)/N$ and $\sigma_\ell^2 = (\sum_i w_i (\ell_i - \bar{\ell})^2)/N$ are weighted average and standard deviation of the *rescaled* spring lengths. This means that $\bar{\ell}$ and σ_ℓ are average and standard deviation of the actual spring lengths l_i, *each measured relative to its actual rest length* l_{0i}. In particular, the standard deviation σ_ℓ vanishes whenever all springs i have the same value of the *fraction* l_i/l_{0i}, even though the absolute lengths l_i may differ among the springs. Moreover, importantly, the mean rest length ℓ_0 enters the definitions of $\bar{\ell}$ and σ_ℓ, but only via the ratios l_{0i}/ℓ_0, which characterize the *relative* spring length distribution. Hence, the "rescaled" geometric information contained in both $\bar{\ell}$ and σ_ℓ is a combination of the actual spring lengths and the *relative* rest length distribution, but is independent of the *absolute* mean rest length ℓ_0.

According to Eq. (5), energy minimization corresponds to a simultaneous minimization with respect to $|\bar{\ell} - \ell_0|$ and σ_ℓ: In the floppy regime we find numerically that both quantities can vanish simultaneously and thus, all lengths attain their rest lengths, $\ell_i = \ell_0$ (Supplemental Information, section IIA). In contrast in the rigid regime, $|\bar{\ell} - \ell_0|$ and σ_ℓ cannot both simultaneously vanish, creating tensions $2(\ell_i - \ell_0)$, which are sufficient to rigidify the network. The transition point ℓ_0^* corresponds to the smallest possible preferred spring length ℓ_0 for which the system can still be floppy. In other words, it corresponds to a local minimum in the average rescaled spring length $\ell_0^* = \min \bar{\ell}$ of the network under the constraint of no fluctuations of the rescaled lengths, $\sigma_\ell = 0$. Because this minimization is with respect to all node positions and includes all springs, it defines the distribution of transition points ℓ_0^* as a collective property of the rescaled geometry of 2D spring networks.

For the cellular models with $k_A > 0$, we analogously find that the transition point is given by the minimal cell perimeter $\bar{\ell}$ (surface in 3D) under the constraint of no cell perimeter *and area fluctuations* $\sigma_\ell = \sigma_a = 0$, which now additionally appear in the energy Eq. (5) (46). Again, this is a geometric criterion, which also explains why the transition point ℓ_0^* is independent of k_A for $k_A > 0$ (Figure 1d,f). Moreover, we can understand why the transition point is smaller for $k_A = 0$: in this case the energy does not constrain the area fluctuations, and the transition point is given by the minimal perimeter under the weaker constraint of having no perimeter fluctuations. Thus, the transition point will generally be smaller for the $k_A = 0$ case than for the $k_A > 0$ case.

B. The minimal length scales linearly with fluctuations. We next study the scaling of the minimal length in the rigid vicinity of the transition. In the rigid regime, the system must compromise between minimizing $|\bar{\ell} - \ell_0|$ and σ_ℓ (and possibly σ_a in cellular models). To understand how, we must account for geometric constraints, which we express in terms of how the minimal length $\bar{\ell}_{\min} = \min \bar{\ell}$ depends on the fluctuations: $\bar{\ell}_{\min} = \bar{\ell}_{\min}(\sigma_\ell, \sigma_a)$. In the rigid regime the observed average length is always greater than the preferred length, $\bar{\ell} > \ell_0$, and so the average length instead takes on its locally minimal possible value $\bar{\ell} = \bar{\ell}_{\min}(\sigma_\ell, \sigma_a)$. Therefore, knowing the functional form of $\bar{\ell}_{\min}(\sigma_\ell, \sigma_a)$ will allow us to predict how the system energy e (and thus also the bulk and shear moduli) depend on the control parameter ℓ_0 (Supplemental Information, section IC-E).

In section IB of the supplement, we show analytically that in the absence of prestresses in the floppy regime, the minimal

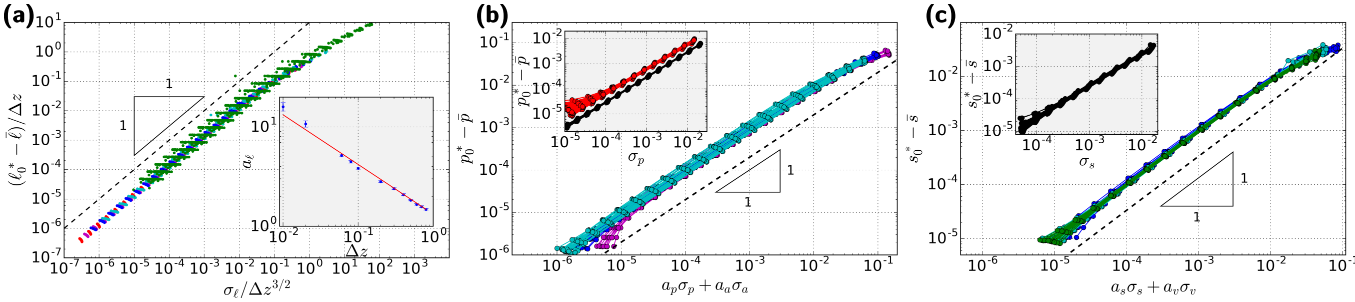

Fig. 2. Verification of the geometric linearity near the transition point. The difference between average length and transition point, $\ell_0^* - \bar{\ell}$, scales linearly with the standard deviations of lengths σ_ℓ and areas σ_a. (a) 2D spring network, (b) 2D Voronoi and vertex models, (c) 3D Voronoi model. The values of z, k_A, and k_V are respectively as in Figure 1. (a inset) For the 2D spring networks, the coefficient a_ℓ in Eq. (6) scales with the distance to isostaticity approximately as $a_\ell \sim \Delta z^{-1/2}$. In all panels, deviations from linearity exist for large $\ell_0^* - \bar{\ell}$ because Eq. (6) and Eq. (7) describe the behavior close to the transition point, and deviations for small $\ell_0^* - \bar{\ell}$ are due the finite cutoff on the shear modulus used to obtain the transition point value ℓ_0^* (Supplemental Information, section IV).

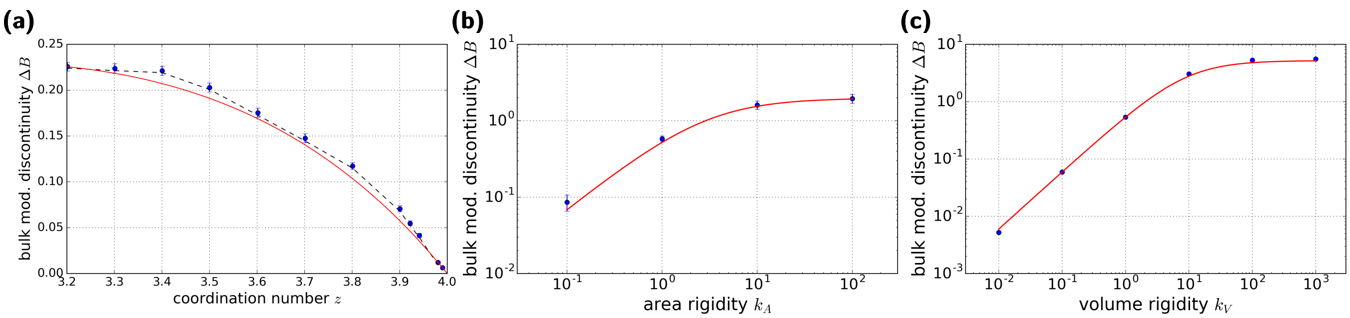

Fig. 3. Predicted and observed behavior of the bulk modulus discontinuity ΔB for (a) 2D spring networks for different values of the coordination number z, (b) the 2D vertex model for different values of the area rigidity k_A and (c) the 3D Voronoi model for different values of the volume rigidity k_V. Blue dots indicate simulations and the red curves indicate predictions without fit parameters based on Eq. (9). In panel a, the black dashed curve is computed using values for transition point ℓ_0^* and geometric scaling coefficient a_ℓ directly measured for each value of z, while for the red line we used the scaling relations from Table 1.

length $\bar{\ell}_{\min}$ depends linearly on the standard deviations σ_ℓ and σ_a. This is directly related to the state of self-stress that is created at the onset of geometric incompatibility at $\ell_0 = \ell_0^* \equiv \bar{\ell}_{\min}(0,0)$ (3).

To check this prediction, we numerically simulate these models, and observe indeed a linear scaling of the $\bar{\ell}_{\min}(\sigma_\ell)$ functions close to the transition point (Figure 2). In particular, for 2D spring networks and the $k_A = 0$ cases of the cellular models, we find:

$$\bar{\ell}_{\min}(\sigma_\ell) = \ell_0^* - a_\ell\sigma_\ell \qquad [6]$$

with scaling coefficient a_ℓ. We list its value in Table 1 for the different models. Interestingly, we find that the coefficient a_ℓ is largely independent of the random realization of the system, in particular for cellular models with $k_A = 0$.

For 2D spring networks, a_ℓ depends on the coordination number z and approximately scales as $a_\ell \sim \Delta z^{-1/2}$ (Figure 2a inset). This scaling behavior of a_ℓ can be rationalized using a scaling argument based on the density of states (Supplemental Information, section IF).

For cellular models where area plays a role, Eq. (6) is extended (Figure 2b,c):

$$\bar{\ell}_{\min}(\sigma_\ell, \sigma_a) = \ell_0^* - a_\ell\sigma_\ell - a_a\sigma_a. \qquad [7]$$

Again the coefficients a_ℓ and a_a are listed in Table 1 for 2D vertex and 3D Voronoi models. The coefficients a_ℓ differ significantly between the $k_A > 0$ and $k_A = 0$ cases of the same model, which makes sense because Eq. (6) and Eq. (7) are linear expansions of the function $\bar{\ell}_{\min}(\sigma_\ell, \sigma_a)$ at different points (σ_ℓ, σ_a).

C. Prediction of the bulk modulus discontinuity. Knowing the behavior of the minimal length function $\bar{\ell}_{\min}(\sigma_\ell, \sigma_a)$ in the rigid phase near the transition point provides us with an explicit expression for the energy in terms of the control parameter ℓ_0 (Supplemental Information, section IC):

$$e(\ell_0) = \frac{N}{Z}(\ell_0^* - \ell_0)^2 \qquad [8]$$

with $Z = 1 + a_\ell^2 + a_a^2/k_A$, where for models without an area term the a_a^2/k_A term is dropped. Because changes in ℓ_0 correspond to changes in system size, we can predict the exact value of the bulk modulus discontinuity, ΔB, at the transition in all models (Figure 1a-c, Supplemental Information, section IE):

$$\Delta B = \frac{2d^2(\ell_0^*)^2}{D^2 Z}. \qquad [9]$$

This equation is for a model with d-dimensional "lengths" embedded in a D-dimensional space (see Table 1). For the special case of a hexagonal lattice in the 2D vertex model, this result is consistent with Ref. (56). More generally, for disordered networks the geometric coefficients a_ℓ and a_a appear in the denominator, because they describe non-affinities that occur in response to global isotropic deformations (Supplemental Information, section IE). A comparison of the predicted ΔB to simulation results is shown in Figure 3.

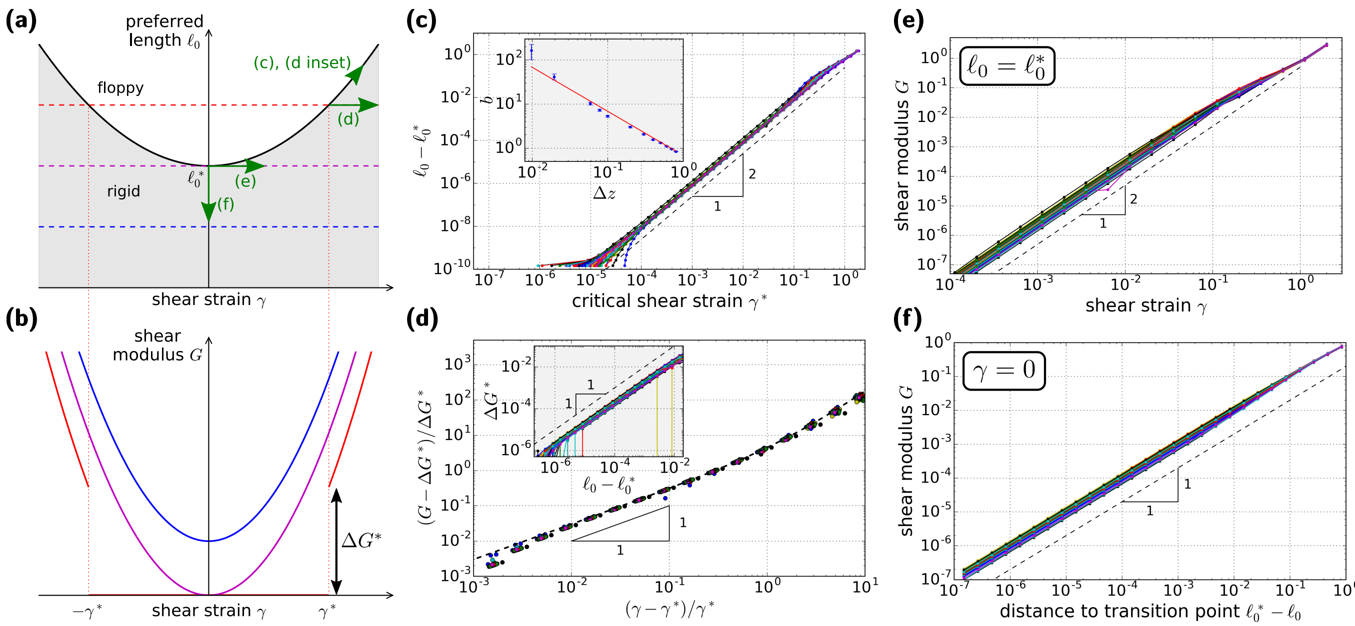

Fig. 4. Nonlinear elastic behavior of sub-isostatic spring networks under shear. (a) Schematic phase diagram illustrating the parabolic boundary between rigid (shaded) and floppy (unshaded) regime depending on preferred spring length ℓ_0 and shear strain γ. (b) Schematic showing the dependence of the shear modulus G on the shear strain γ for different values of ℓ_0 (cf. panel a). Note that for $\ell_0 > \ell_0^*$ (red curve), Eq. (12) predicts a discontinuity ΔG^* in the shear modulus at the onset of rigidity. (c) We numerically find a quadratic dependence between $\ell_0 - \ell_0^*$ and the critical shear γ^* where the network rigidifies for given $\ell_0 > \ell_0^*$. This is consistent with our Taylor expansion in Eq. (10), and the quadratic regime extends to shear strains of up to $\gamma \sim 0.1$. Deviations for very small $\ell_0 - \ell_0^*$ are attributed to the finite shear modulus cutoff of 10^{-10} used to probe the phase boundary (Supplemental Information, section IVB). (c inset) The prefactor b associated with the quadratic relation in panel c scales approximately as $b \sim 1/\Delta z$. (d) Scaling of the shear modulus beyond the shear modulus discontinuity, $(G - \Delta G^*)/\Delta G^*$ over $(\gamma - \gamma^*)/\gamma^*$ with $\ell_0 - \ell_0^* = 10^{-4}$. The dashed black line indicates the prediction from Eq. (12) without fit parameters. (d inset) Scaling of the shear modulus discontinuity ΔG^* with $\ell_0 - \ell_0^*$. (e,f) Scaling of the shear modulus with γ and $\ell_0^* - \ell_0$, respectively. In all panels the coordination number is $z = 3.2$.

D. Nonlinear elastic behavior under shear. As shown before (8–10, 12, 14–16, 18–21), under-constrained systems can also be rigidified by applying finite shear strain. We now incorporate shear strain γ into our formalism and test our predictions on the 2D spring networks. However, we expect our findings to equally apply to the cell-based models (Supplemental Information, section IC,D). We also numerically verified that our analytical predictions also apply to 2D fiber networks without bending rigidity (Supplemental Information, section IIC).

To extend our approach, we take into account that the minimal-length function $\bar{\ell}_{\min}(\sigma_\ell)$ can in principle also depend on the shear strain γ. We thus Taylor expand in γ:

$$\bar{\ell}_{\min}(\sigma_\ell, \gamma) = \ell_0^* - a_\ell \sigma_\ell + b\gamma^2, \qquad [10]$$

where the linear term in γ is dropped due to symmetry when expanding about an isotropic state (in practice, for our finite-sized systems we drop the linear term in γ by defining the $\gamma = 0$ point using shear stabilization, Supplemental Information, sections ID and IV). While at the moment we have no formal proof that $\ell_{\min}$ is analytic, and the ultimate justification for Eq. (10) comes from a numerical check (see next paragraph), we hypothesize that for most systems $\ell_{\min}$ will be analytic in γ, up to randomly scattered points γ where singularities in the form of plastic rearrangements occur.

For a fixed value of γ, the interface between solid and rigid regime is again given by $\bar{\ell}_{\min}(\sigma_\ell = 0, \gamma)$, and the corresponding phase diagram in terms of both control parameters γ and ℓ_0 is illustrated in Figure 4a. Indeed, we also numerically find a quadratic scaling for the transition line, $\ell_0 - \ell_0^* = b(\gamma^*)^2$, extending up to shear strains of $\gamma \sim 0.1$ (Figure 4c, see also Supplemental Information, section IIB). We find that for spring networks the coefficient b depends on Δz approximately as $b \sim \Delta z^{-1}$ (Figure 4c inset), which can be understood from properties of the density of states (Supplemental Information, section IF). To optimize precision, values of b have been extracted from the relation $G = 4b(\bar{\ell} - \ell_0)$ in this plot (see below, cf. Figure 4f).

Knowing the functional form of $\bar{\ell}_{\min}(\sigma_\ell, \gamma)$ close to the transition line allows us to explicitly express the energy in the rigid regime in terms of both control parameters (Supplemental Information, section IC):

$$e(\ell_0, \gamma) = \frac{N}{1 + a_\ell^2}\left(\ell_0^* - \ell_0 + b\gamma^2\right)^2. \qquad [11]$$

This allows us to explicitly compute the shear modulus $G = (\mathrm{d}^2 e/\mathrm{d}\gamma^2)/N$. We obtain for both floppy and rigid regime:

$$G(\ell_0, \gamma) = \Theta\left(\ell_0^* - \ell_0 + b\gamma^2\right)\frac{4b}{1 + a_\ell^2}\left(\ell_0^* - \ell_0 + 3b\gamma^2\right), \qquad [12]$$

where Θ is the Heaviside function. We now discuss several consequences of this expression for the shear modulus (Figure 4b).

When shearing the system starting in the floppy regime (i.e. for $\ell_0 > \ell_0^*$), Eq. (12) predicts a *discontinuous* change in the shear modulus of $\Delta G^* = 8b(\ell_0 - \ell_0^*)/(1 + a_\ell^2)$ at the onset of rigidity at $\gamma^* = [(\ell_0 - \ell_0^*)/b]^{1/2}$. We verify the linear scaling $\Delta G^* \sim (\ell_0 - \ell_0^*)$ in Figure 4d inset, and the value of the scaling coefficient in the Supplemental Information, section IIB. Moreover, Eq. (12) also correctly predicts the behavior beyond γ^*, as shown in Figure 4d.

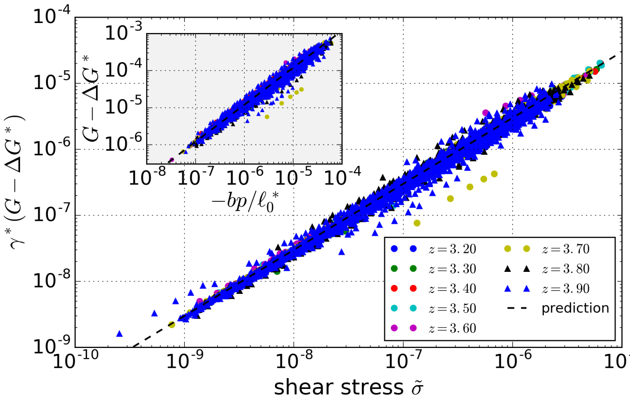

Fig. 5. The excess shear modulus $G-\Delta G^*$ scales linearly with the shear stress $\tilde{\sigma}$ in 2D spring networks. We find a collapse when rescaling $G-\Delta G^*$ by the critical shear strain γ^*. The black dashed line corresponds to the prefactor of 3, as predicted by Eq. (13). (inset) The excess shear modulus $G-\Delta G^*$ scales linearly with the isotropic stress $-p$, and we obtain a collapse when rescaling the latter by b/ℓ_0^*. The black dashed line is the prediction according to Eq. (13).

Eq. (12) also correctly predicts the shear modulus behavior for $\ell_0 \le \ell_0^*$. For $\ell_0 = \ell_0^*$, the shear modulus scales quadratically with γ (Figure 4e), while for $\gamma = 0$, the shear modulus scales linearly with $(\ell_0^* - \ell_0) > 0$ (Figure 4f, see Supplemental Information, section ID, for the cellular models), as reported before for many of the cellular models (37, 46, 56). In both cases, we verified that the respective coefficients coincide with their expected values based on the values of a_ℓ and b.

In particular for $\gamma = 0$, because $(\ell_0^* - \ell_0) = (1 + a_\ell^2)(\bar{\ell} - \ell_0)$, we obtain the simple relation $G = 4b(\bar{\ell} - \ell_0)$, which explains the collapse in the shear modulus scaling for different k_V in the 3D Voronoi model that some of us reported earlier (46).

We also obtain explicit expressions for both shear stress $\tilde{\sigma} = (\mathrm{d}e/\mathrm{d}\gamma)/N$ and isotropic stress, i.e. negative pressure $-p$ (Supplemental Information, sections ID,E). For the latter, we find a negative Poynting effect with coefficient $\chi \equiv p/\gamma^2 = -2db\ell_0^*/D(1 + a_\ell^2)$ at $\ell_0 = \ell_0^*$. Moreover, we find the following relations for the shear modulus:

$$G = \Delta G^* + \frac{3}{\gamma}\tilde{\sigma} \qquad\qquad G = \Delta G^* - \frac{6Db}{d\ell_0^*}p. \qquad [13]$$

Indeed, we observe a collapse of our simulation data for the 2D spring networks in both cases (Figure 5 & inset), where we use that close to the onset of rigidity, $\gamma \simeq \gamma^*$.

Discussion

In this article, we propose a unifying perspective on under-constrained materials that are stiffened by geometric incompatibility. This is relevant for a broad class of materials (6), and has more recently been discussed in the context of biopolymer gels (8, 12–14, 21) and biological tissues (31, 37, 42, 46). Just as with a guitar string, we are able to predict many features of the mechanical response of these systems by quantifying geometric incompatibility – we develop a generic geometric rule $\bar{\ell}_{\min}$ for how generalized springs in a disordered network deviate from their rest length. Using this minimal average length function $\bar{\ell}_{\min}$, we then derive the macroscopic elastic properties of a very broad class of under-constrained, prestress-rigidified materials from first principles. We numerically verify our findings using models for biopolymer networks (9, 14) and biological tissues (34, 38, 46).

Our work is relevant for experimentalists and may explain the reproducibility of a number of generic mechanical features found in particular for biopolymer networks (12, 17, 21, 25). While we neglect here a fiber bending rigidity that is included in many biopolymer network models (12–15, 21), future work that includes such a term will further refine our theoretical results and the following comparison to experiments (see below). For shear deformations with ℓ_0 sufficiently close to ℓ_0^* and close to the onset of rigidity $\gamma \simeq \gamma^*$, we predict a linear scaling of the differential shear modulus G with the shear stress $\tilde{\sigma}$, where $(G - \Delta G^*)/\tilde{\sigma} \sim 1/\gamma^*$, which has been reported before for biopolymer networks (12, 13, 21). However, here we additionally predict from first principles that the value of the prefactor is exactly 3, a factor consistent with previous experimental results (12, 21). Moreover, our work strongly suggests that the relation $(G - \Delta G^*)/\tilde{\sigma} = 3/\gamma$ is a general hallmark of prestress-induced rigidity in under-constrained materials. We thus propose it as a general experimental criterion to test whether an observed strain-stiffening behavior can be understood in terms of geometrically induced rigidity. If applicable to biopolymer gels, this could help to discern whether strain-stiffening of a gel is due to the nonlinear mechanics of single filaments or is dominated by prestresses, a long-standing question in the field (8, 57).

We can also apply these predictions to typical rheometer geometries (Supplemental Information, section IG). We predict that an atypical tensile normal stress σ_{zz} develops under simple shear, which corresponds to a negative Poynting effect, that σ_{zz} scales linearly with shear stress and shear modulus: $\sigma_{zz} \sim \tilde{\sigma} \sim (G - \Delta G^*)$ (Eq. (13) and Supplemental Information, section IG). This is precisely what has been found for many biopolymer gels like collagen, fibrin, or matrigel (12, 21, 25, 26). However, in contrast to Ref. (21), our work suggests that the scaling factor between σ_{zz} and $(G - \Delta G^*)$ should be largely independent of γ^*. While these effects can also be explained by nonlinearities (25, 57–59), and have already been discussed in the context of prestress-induced rigidity (13, 19, 21), we show here that they represent a very generic feature of prestress-induced rigidity in under-constrained materials.

Our work also highlights the importance of isotropic deformations when studying prestress-induced rigidity, as demonstrated experimentally in Ref. (17). While previous work (8, 9, 12, 14, 15, 18, 20, 21) focused almost (10) entirely on shear deformations, we additionally study the effect of isotropic deformations represented by the control parameter ℓ_0. First, due to the bulk modulus discontinuity, our work predicts zero normal stress under compression and linearly increasing normal stress under expansion, consistent with experimental findings on biopolymer networks (17) (assuming the uniaxial response is dominated by the isotropic part of the stress tensor, see Supplemental Information, section IG). Second, we also correctly predict that the critical shear strain γ^* increases upon compression, which corresponds to an increase in ℓ_0 (17) (cf. Figure 4a). While we also predict an increase of the shear modulus G under extension, which was observed as well (17), additional effects arising from the superposition of pure shear and simple shear very likely play an important role in this case. While we consider this outside the scope of this article, it will be straight-forward to extend our work by this aspect.

In summary, we have developed a new approach to understand how many under-constrained disordered materials rigidify in a manner similar to a guitar string. While it is clear that the one-dimensional string becomes rigid precisely when it is stretched past its rest length, we show that in two- and three-dimensional models, rigidity is governed by a geometrical minimal length function $\bar{\ell}_{\min}$ with generic features (e.g. linear scaling with intrinsic fluctuations, quadratic scaling with shear strain). This insight allows us to make accurate predictions for many of the scaling functions and prefactors that describe the linear response of these materials. In addition, by performing numerical measurements of the geometry in the rigid phase to extract the coefficients of the $\bar{\ell}_{\min}$ function, we can even predict the precise magnitudes of several macroscopic mechanical properties.

In addition, these predictions help unify or clarify several scaling collapses that have been identified previously in the literature. For 2D spring networks derived from jammed packings, we studied the dependence of our geometric coefficients on the coordination number z, and find that approximately, $a_\ell \sim \Delta z^{-1/2}$ and $b \sim \Delta z^{-1}$. Combined with our finding that the value of ℓ_0 right after initialization depends linearly on z, such that $(\ell_0 - \ell_0^*) \sim \Delta z$ (Figure S5a inset in the Supplemental Information), we obtain that the critical shear strain γ^* scales as $\gamma^* \sim \Delta z^\beta$ with $\beta = 1$. Similarly, we find for the associated shear modulus discontinuity $\Delta G^* \sim \Delta z^\theta$ with $\theta = 1$. While both exponents are consistent with earlier findings by Wyart et al. (9), our approach highlights the importance of the initial value of ℓ_0 for the elastic properties under shear. In other work, bond-diluted regular networks yielded different exponents β and θ (16), which is not surprising because the scaling exponents of a_ℓ and b with Δz are likely dependent on the way the network is generated. More generally, while we observed that the values of ℓ_0^*, a_ℓ, a_a, and b depended somewhat on the protocol of system preparation and energy minimization, they were relatively reproducible among different random realizations of a given protocol (55).

Moreover, we analytically predict and numerically confirm the existence and precise value of a shear modulus discontinuity ΔG^* with respect to shear deformation, whose existence for fiber networks without bending rigidity has been controversially discussed more recently (14, 15, 18, 20, 24). We also predict a generic scaling of the shear modulus beyond this discontinuity: $(G - \Delta G^*) \sim (\gamma - \gamma^*)^f$ with $f = 1$. Smaller values for f that have been reported before for different kinds of spring and fiber networks (14, 15, 18, 20) are likely due to higher order terms in $\bar{\ell}_{\min}$. Given the very generic nature of our approach, we expect to find a value of $f = 1$ in these systems as well, if probed sufficiently close to $\ell_0 = \ell_0^*$.

One major obstacle in determining elastic properties of disordered materials is the appearance of non-affinities, which can lead to a break-down of approaches like effective medium theory close to the transition (10). In our case, effects by non-affinities are by construction fully included in the geometric coefficients a_ℓ, a_a, and b. However, while measures for non-affinity have been discussed before (9, 15, 20, 28, 60), these are usually quite distinct from our coefficients a_ℓ, a_a, and b. For example for spring networks, such earlier definitions typically include spring *rotations*, while our coefficients represent changes in spring *length* only. Hence, while earlier definitions reflect much of the actual *motion* of the microscopic elements, our coefficients only retain the part directly relevant for the system energy and thus the mechanics. In other words, the coefficients a_ℓ, a_a, and b (and ℓ_0^*) can be regarded as a minimal set of parameters required to characterize the elastic system properties close to the transition.

There are a number of possible future extensions of this work. First, we have focused here on transitions created by a minimal length, where the system is floppy for large ℓ_0 and rigid for small ℓ_0. However, there is in principle also the possibility of a transition created by e.g. a maximal length, which is for example the case in classical sphere jamming. Although we have occasionally seen something like this in our spring networks close to isostaticity, we generally expect this to be less typical in under-constrained systems due to buckling.

Second, while we studied here the vicinity of one local minimum of $\bar{\ell}_{\min}$ depending e.g. on γ, it would be interesting to study the behavior of the system beyond that, by including higher order terms in $\bar{\ell}_{\min}$, and by also explicitly taking plastic events into account (61). In the case of biological tissues, plastic events typically correspond to so-called T1 transitions (62), which in our approach would correspond to changing to a different $\bar{\ell}_{\min}$ "branch".

Third, it will be important to study what determines the exact values of the geometric coefficients a_ℓ, a_a, and b, how they depend on the network statistics, and why they are relatively reproducible. For the cellular models with area term, preliminary results suggest that the ratio of both "a" coefficients can be estimated by $a_a/a_\ell \approx d\ell_0^*/D$, because the self-stress that appears at the onset of rigidity seems to be dominated by a force balance between cell perimeter tension and pressure within each cell.

Fourth, because we separated geometry from energetics, it is in principle possible to generalize our work to other interaction potentials, e.g. the correct expression for semiflexible filaments (57, 59), and to include the effect of active stresses (54, 63–65). Note that our work directly generalizes to any analytic interaction potential with a local minimum at a finite length. Although in this more general case Eq. (5) would include higher order cumulants of ℓ_i, these higher order terms will be irrelevant in the floppy regime and we expect them to be negligible in the rigid vicinity of the transition, where we make most of our predictions.

Fifth, this work may also provide foundations to systematically connect macroscopic mechanical material properties to the underlying *local* geometric structure. For example for biopolymer networks, properties of the local geometric structure can be extracted using light scattering, scanning electron microscopy, or confocal reflectance microscopy (21, 66, 67). In particular, our simulations indicate that in models without area term the $\bar{\ell}_{\min}$ function does not change much when increasing system size by nearly an order of magnitude (Supplemental Information, section IID), which suggests that local geometry may indeed be sufficient to characterize the large-scale mechanical properties of such systems. Remaining future challenges here include the development of an easy way to compute our geometric coefficients from simple properties characterizing local geometric structure without the need to simulate, and to find ways to detect possible residual stresses that may have been built into the gel during polymerization.

Finally, our approach can likely be extended to also include isostatic and over-constrained materials. For example, it is generally assumed that the mechanics of biopolymer networks is dominated by a stretching rigidity of fibers that form a sub-isostatic network, but that an additional fiber bending rigidity turns the network into an over-constrained system (12–15, 21, 22). The predictions we make here focus on the stretching-dominated limit where fiber bending rigidity can be neglected, which is attained by a weak fiber bending modulus and/or in the more rigid parts of the phase space. A generalization of our formalism towards over-constrained systems will allow us to extend our predictions beyond this regime and thus refine our comparison to experimental data.

Materials and Methods

Numerical implementation of the models. The 2D spring networks were initialized as packing-derived, randomly cut networks (9, 27). To improve the precision as compared to the cellular models, we created our own implementation of the Polak-Ribière version of the conjugate gradient minimization method (68), where for the line searches we use a self-developed Newton method based only on energy derivatives. All states were minimized until the average force per degree of freedom was less than 10^{-12}. For the ℓ_0 sweep in Figure 1a,b and to find the $(\gamma, \ell_0) = (0, \ell_0^*)$ point, we used shear stabilization. Details are given in section IVB of the Supplemental Information.

For the 2D vertex model simulations, we always started from Voronoi tessellations of random point patterns, generated using the Computational Geometry Algorithms Library (CGAL, https://www.cgal.org/), and we used the BFGS2 implementation of the GNU Scientific Library (GSL, https://gnu.org/software/gsl/) to minimize the energy. We enforced 3-way vertices and the length cutoff for T1 transitions was set to 10^{-5}, and there is a maximum possible number of T1 transitions on a single cell-cell interface of 10^4. All 2D vertex model configurations studied were shear stabilized.

For the 2D Voronoi model simulations, we started from random point patterns and minimized the system energy using the BFGS2 routine of the GSL, each time using CGAL to compute the Voronoi tessellations. Due to limitations of CGAL, configurations were not shear stabilized.

For the 3D Voronoi model simulations, we used the shear-stabilized, energy-minimized states generated in Ref. (46) using the BFGS2 multidimensional minimization routine of the GSL.

Details on the different simulation protocols (ℓ_0 sweeps and bisection to obtain the transition point) are discussed in detail in section IV of the Supplemental Information.

ACKNOWLEDGMENTS. We thank Daniel M. Sussman for fruitful discussions. MM and MLM acknowledge funding from the Simons Foundation under grant number 446222, the Alfred P. Sloan Foundation, the Gordon and Betty Moore Foundation, the Research Corporation for Scientific Advancement though the Cottrell Scholars program, and computational support through NSF ACI-1541396. MLM also acknowledges support from the Simons Foundation under grant number 454947, and NSF-DMR-1352184 and NSF-PHY-1607416. KB and BPT acknowledge funding from the Netherlands Organization for Scientific Research (NWO).

1. Maxwell JC (1864) On the calculation of the equilibrium and stiffness of frames. *Philosophical Magazine Series 4* 27(182):294–299.
2. Calladine CR (1978) Buckminster Fuller's "Tensegrity" structures and Clerk Maxwell's rules for the construction of stiff frames. *International Journal of Solids and Structures* 14(2):161–172.
3. Lubensky TC, Kane CL, Mao X, Souslov A, Sun K (2015) Phonons and elasticity in critically coordinated lattices. *Reports on Progress in Physics* 78(7):73901.
4. Zhou D, Zhang L, Mao X (2018) Topological Edge Floppy Modes in Disordered Fiber Networks. *Physical Review Letters* 120(6):68003.
5. Mao X, Lubensky TC (2018) Maxwell Lattices and Topological Mechanics. *Annu. Rev. Condens. Matter Phys* 9:413–33.
6. Alexander S (1998) Amorphous solids: Their structure, lattice dynamics and elasticity. *Physics Report* 296(2-4):65–236.
7. Ingber DE, Wang N, Stamenović D (2014) Tensegrity, cellular biophysics, and the mechanics of living systems. *Reports on Progress in Physics* 77(4):046603.
8. Onck PR, Koeman T, van Dillen T, van der Giessen E (2005) Alternative Explanation of Stiffening in Cross-Linked Semiflexible Networks. *Physical Review Letters* 95(17):178102.
9. Wyart M, Liang H, Kabla A, Mahadevan L (2008) Elasticity of floppy and stiff random networks. *Physical Review Letters* 101(21):1–4.
10. Sheinman M, Broedersz CP, MacKintosh FC (2012) Nonlinear effective-medium theory of disordered spring networks. *Physical Review E* 85(2):021801.
11. Silverberg JL, et al. (2014) Structure-Function Relations and Rigidity Percolation in the Shear Properties of Articular Cartilage. *Biophysical Journal* 107(7):1721–1730.
12. Licup AJ, et al. (2015) Stress controls the mechanics of collagen networks. *Proceedings of the National Academy of Sciences* 112(31):9573–9578.
13. Licup AJ, Sharma A, MacKintosh FC (2016) Elastic regimes of subisostatic athermal fiber networks. *Physical Review E* 93(1):012407.
14. Sharma A, et al. (2016) Strain-controlled criticality governs the nonlinear mechanics of fibre networks. *Nature Physics* 12(6):584–587.
15. Sharma A, et al. (2016) Strain-driven criticality underlies nonlinear mechanics of fibrous networks. *Physical Review E* 94(4):042407.
16. Feng J, Levine H, Mao X, Sander LM (2016) Nonlinear elasticity of disordered fiber networks. *Soft Matter* 12(5):1419–1424.
17. van Oosten ASG, et al. (2016) Uncoupling shear and uniaxial elastic moduli of semiflexible biopolymer networks: compression-softening and stretch-stiffening. *Scientific Reports* 6(1):19270.
18. Vermeulen MFJ, Bose A, Storm C, Ellenbroek WG (2017) Geometry and the onset of rigidity in a disordered network. *Physical Review E* 96(5):053003.
19. Shivers J, Feng J, Sharma A, MacKintosh FC (2017) Anomalous normal stress controlled by marginal stability in fiber networks. *arXiv:1711.00522*.
20. Shivers J, Arzash S, Sharma A, MacKintosh FC (2018) Scaling theory for mechanical critical behavior in fiber networks. *arXiv:1807.01205* (c).
21. Jansen KA, et al. (2018) The Role of Network Architecture in Collagen Mechanics. *Biophysical Journal* 114(11):2665–2678.
22. Rens R, Villarroel C, Düring G, Lerner E (2018) Micromechanical theory of strain-stiffening of biopolymer networks. *arXiv:1808.04756*.
23. Rammensee S, Janmey PA, Bausch AR (2007) Mechanical and structural properties of in vitro neurofilament hydrogels. *European Biophysics Journal* 36(6):661–668.
24. Rens R, Vahabi M, Licup AJ, MacKintosh FC, Sharma A (2016) Nonlinear Mechanics of Athermal Branched Biopolymer Networks. *The Journal of Physical Chemistry B* 120(26):5831–5841.
25. Janmey PA, et al. (2007) Negative normal stress in semiflexible biopolymer gels. *Nature Materials* 6(1):48–51.
26. de Cagny HCG, et al. (2016) Porosity Governs Normal Stresses in Polymer Gels. *Physical Review Letters* 117(21):217802.
27. Baumgarten K, Tighe BP (2018) Normal Stresses, Contraction, and Stiffening in Sheared Elastic Networks. *Physical Review Letters* 120(14):148004.
28. Broedersz CP, Mao X, Lubensky TC, MacKintosh FC (2011) Criticality and isostaticity in fibre networks. *Nature Physics* 7(12):983–988.
29. Angelini TE, et al. (2011) Glass-like dynamics of collective cell migration. *Proceedings of the National Academy of Sciences* 108(12):4714–4719.
30. Sadati M, Taheri Qazvini N, Krishnan R, Park CY, Fredberg JJ (2013) Collective migration and cell jamming. *Differentiation* 86(3):121–125.
31. Park JA, et al. (2015) Unjamming and cell shape in the asthmatic airway epithelium. *Nature Materials* 14(10):1040–1048.
32. Garcia S, et al. (2015) Physics of active jamming during collective cellular motion in a monolayer. *Proceedings of the National Academy of Sciences* 112(50):15314–15319.
33. Malinverno C, et al. (2017) Endocytic reawakening of motility in jammed epithelia. *Nature Materials* 16(5):587–596.
34. Farhadifar R, Röper JC, Aigouy B, Eaton S, Jülicher F (2007) The Influence of Cell Mechanics, Cell-Cell Interactions, and Proliferation on Epithelial Packing. *Current Biology* 17(24):2095–2104.
35. Staple DB, et al. (2010) Mechanics and remodelling of cell packings in epithelia. *The European Physical Journal E* 33(2):117–127.
36. Bi D, Lopez JH, Schwarz JM, Manning ML (2014) Energy barriers and cell migration in densely packed tissues. *Soft Matter* 10(12):1885.
37. Bi D, Lopez JH, Schwarz JM, Manning ML (2015) A density-independent rigidity transition in biological tissues. *Nature Physics* 11(12):1074–1079.
38. Bi D, Yang X, Marchetti MC, Manning ML (2016) Motility-Driven Glass and Jamming Transitions in Biological Tissues. *Physical Review X* 6(2):021011.
39. Matoz-Fernandez DA, Martens K, Sknepnek R, Barrat JL, Henkes S (2017) Cell division and death inhibit glassy behaviour of confluent tissues. *Soft Matter* 13(17):3205–3212.
40. Barton DL, Henkes S, Weijer CJ, Sknepnek R (2017) Active Vertex Model for cell-resolution description of epithelial tissue mechanics. *PLOS Computational Biology* 13(6):e1005569.
41. Yang X, et al. (2017) Correlating Cell Shape and Cellular Stress in Motile Confluent Tissues. *Proceedings of the National Academy of Sciences* 114(48):12663–12668.
42. Moshe M, Bowick MJ, Marchetti MC (2017) Geometric frustration and solid-solid transitions in model 2D tissue. *Physical Review Letters* 120(26):268105.
43. Giavazzi F, et al. (2018) Flocking Transitions in Confluent Tissues. *Soft Matter*.
44. Sussman DM, Merkel M (2018) No unjamming transition in a Voronoi model of biological tissue. *Soft Matter*.
45. Sussman DM, Paoluzzi M, Cristina Marchetti M, Lisa Manning M (2018) Anomalous glassy dynamics in simple models of dense biological tissue. *EPL (Europhysics Letters)* 121(3):36001.
46. Merkel M, Manning ML (2018) A geometrically controlled rigidity transition in a model for confluent 3D tissues. *New Journal of Physics* 20(2):022002.
47. Boromand A, Signoriello A, Ye F, O'Hern CS, Shattuk M (2018) Jamming of Deformable Polygons. *arXiv:1801.06150*.

48. Yan L, Bi D (2018) Rosette-driven rigidity transition in epithelial tissues. *arXiv:1806.04388*.
49. Teomy E, Kessler DA, Levine H (2018) Confluent and non-confluent phases in a model of cell tissue. *arXiv:1803.03962* (2).
50. Tighe BP (2012) Dynamic critical response in damped random spring networks. *Physical Review Letters* 109(16):168303.
51. Yucht M, Sheinman M, Broedersz C (2013) Dynamical behavior of disordered spring networks. *Soft Matter* 9(29):7000–7006.
52. Düring G, Lerner E, Wyart M (2013) Phonon gap and localization lengths in floppy materials. *Soft Matter* 9(1):146–154.
53. Düring G, Lerner E, Wyart M (2014) Length scales and self-organization in dense suspension flows. *Physical Review E* 89(2):022305.
54. Woodhouse FG, Ronellenfitsch H, Dunkel J (2018) Autonomous actuation of zero modes in mechanical networks far from equilibrium. *arXiv:1805.07728*.
55. Chaudhuri P, Berthier L, Sastry S (2010) Jamming transitions in amorphous packings of frictionless spheres occur over a continuous range of volume fractions. *Physical Review Letters* 104(16):165701.
56. Murisic N, Hakim V, Kevrekidis IG, Shvartsman SY, Audoly B (2015) From Discrete to Continuum Models of Three-Dimensional Deformations in Epithelial Sheets. *Biophysical Journal* 109(1):154–163.
57. Storm C, Pastore JJ, MacKintosh FC, Lubensky TC, Janmey PA (2005) Nonlinear elasticity in biological gels. *Nature* 435(7039):191–194.
58. Kang H, et al. (2009) Nonlinear Elasticity of Stiff Filament Networks: Strain Stiffening, Negative Normal Stress, and Filament Alignment in Fibrin Gels †. *The Journal of Physical Chemistry B* 113(12):3799–3805.
59. Cioroianu AR, Storm C (2013) Normal stresses in elastic networks. *Physical Review E* 88(5):052601.
60. Broedersz CP, Sheinman M, MacKintosh FC (2012) Filament-length-controlled elasticity in 3D fiber networks. *Physical Review Letters* 108(7):3–7.
61. Amuasi H, Fischer A, Zippelius A, Heussinger C (2018) Linear rheology of reversibly crosslinked biopolymer networks. *arXiv:1808.05407*.
62. Kim S, Wang Y, Hilgenfeldt S (2018) Universal Features of Metastable State Energies in Cellular Matter. *Physical Review Letters* 120(24):248001.
63. Ronceray P, Broedersz CP, Lenz M (2016) Fiber networks amplify active stress. *Proceedings of the National Academy of Sciences* 113(11):2827–2832.
64. Stam S, et al. (2017) Filament rigidity and connectivity tune the deformation modes of active biopolymer networks. *Proceedings of the National Academy of Sciences* 114(47):E10037–E10045.
65. Fischer-Friedrich E (2018) Active Prestress Leads to an Apparent Stiffening of Cells through Geometrical Effects. *Biophysical Journal* 114(2):419–424.
66. Roeder BA, Kokini K, Sturgis JE, Robinson JP, Voytik-Harbin SL (2002) Tensile Mechanical Properties of Three-Dimensional Type I Collagen Extracellular Matrices With Varied Microstructure. *Journal of Biomechanical Engineering* 124(2):214.
67. Lindström SB, Vader DA, Kulachenko A, Weitz DA (2010) Biopolymer network geometries: Characterization, regeneration, and elastic properties. *Physical Review E* 82(5):051905.
68. Nash SG, Sofer A (1995) *Linear and Nonlinear Programming.* (McGraw-Hill College).

Supplemental Information

A minimal-length approach unifies rigidity in under-constrained materials

Matthias Merkel,[1] Karsten Baumgarten,[2] Brian P. Tighe,[2] and M. Lisa Manning[1]

[1] *Department of Physics, Syracuse University, Syracuse, New York 13244, USA*
[2] *Delft University of Technology, Process & Energy Laboratory, Leeghwaterstraat 39, 2628 CB Delft, The Netherlands*

CONTENTS

I. THE MINIMUM LENGTH FUNCTION $\ell_{\min}$ CONTROLS THE MATERIAL BEHAVIOR

A. System energy in terms of average and standard deviation of the rescaled spring lengths

Here we derive Eqs. (2) and (5) in the main text, starting from Eq. (1), which we restate here:

$$e_{s2D} = \sum_i (l_i - l_{0i})^2. \tag{S1}$$

To derive Eq. (2), we first introduce the mean rescaled spring rest length ℓ_0, together with the rescaled spring lengths ℓ_i and the weights w_i:

$$\ell_0 = \left[\frac{1}{N}\sum_i l_{0i}^2\right]^{1/2} \tag{S2}$$

$$\ell_i = \ell_0 \frac{l_i}{l_{0i}} \tag{S3}$$

$$w_i = \left[\frac{l_{0i}}{\ell_0}\right]^2. \tag{S4}$$

In this subsection, all sums are over all springs i in the network. The rescaled spring length ℓ_i is the actual spring length *measured relative to its rest lengths* and rescaled by ℓ_0. Combining Eqs. (S1), (S3), and (S4), we obtain Eq. (2) in the main text:

$$e_{s2D} = \sum_i w_i(\ell_i - \ell_0)^2. \tag{S5}$$

We now need to show that Eq. (S5) is the same as Eq. (5) in the main text, which reads:

$$e_{s2D} = N\Big[(\bar\ell - \ell_0)^2 + \sigma_\ell^2\Big] \tag{S6}$$

with the following definitions for the (weighted) average and standard deviation of the rescaled spring lengths ℓ_i:

$$\bar\ell = \frac{1}{N}\sum_i w_i \ell_i \tag{S7}$$

$$\sigma_\ell = \left[\frac{1}{N}\sum_i w_i(\ell_i - \bar\ell)^2\right]^{1/2}. \tag{S8}$$

To this end, we first use Eqs. (S4) and (S2) to obtain:

$$\sum_i w_i = N. \tag{S9}$$

This relation is then used to transform σ_ℓ^2 by expanding the square inside of the sum:

$$\sigma_\ell^2 = \frac{1}{N}\sum_i w_i \ell_i^2 - 2\bar\ell \frac{1}{N}\sum_i w_i \ell_i + \bar\ell^2, \tag{S10}$$

and with Eq. (S7):

$$\sigma_\ell^2 = \frac{1}{N}\sum_i w_i \ell_i^2 - \bar\ell^2. \tag{S11}$$

Adding $(\bar{\ell}-\ell_0)^2$ on both sides yields

$$(\bar{\ell}-\ell_0)^2+\sigma_\ell^2=\frac{1}{N}\sum_i w_i\ell_i^2-2\bar{\ell}\ell_0+\ell_0^2, \tag{S12}$$

and using again Eq. (S7):

$$(\bar{\ell}-\ell_0)^2+\sigma_\ell^2=\frac{1}{N}\sum_i w_i(\ell_i-\ell_0)^2. \tag{S13}$$

Hence, Eqs. (2) and (5) in the main text are equivalent.

B. The coefficients a_ℓ and a_a are properties of a self-stress

Here we show that the coefficients a_ℓ and a_a are closely related to the self-stress $\boldsymbol{t}$ that is created at the onset of geometric incompatibility, at $\ell_0=\ell_0^*$ [1]. To this end, we start here by focusing on the case without area term, and where all weights are $w_i=1$ (cf. Eq. (2) in main text). At the end, we explain how to include both heterogeneous weights and area terms. Also, we assume for simplicity that close to the transition point there is only a single self-stress, which is the self-stress created by the onset of geometric incompatibility. However, while some models can only exhibit at most a single self-stress (Section III), we have convinced ourselves that our derivation can also be generalized to the case where several self-stresses are present at ℓ_0^*. Finally, we assume here that there are no prestresses in the floppy regime, which implies that all lengths attain their preferred value right at the transition point. At the end of this section, we briefly discuss exceptions to this assumption. For clarity, we set $\gamma=0$ throughout this section.

A self-stress $\boldsymbol{t}$ is defined by

$$\boldsymbol{t}\cdot\boldsymbol{C}=0, \tag{S14}$$

where $\boldsymbol{C}$ is the compatibility matrix with components $C_{in}=\partial\ell_i/\partial r_n$, with $i=1,\dots,N$ running over all generalized springs with lengths ℓ_i, and n running over all degrees of freedom r_n.

We show here that the creation of a self-stress $\boldsymbol{t}$ at the transition implies a linear scaling of the minimal average length $\bar{\ell}$ with σ_ℓ. Moreover, it even implies such a scaling for each individual spring length ℓ_i. To show this, we first note that – up to a prefactor – any vector $\boldsymbol{t}$ can always be written as:

$$\boldsymbol{t}=\boldsymbol{e}+a_\ell\boldsymbol{m}_t, \tag{S15}$$

where $\boldsymbol{e}=(1,\dots,1)$ and $\boldsymbol{m}_t$ is some vector normalized such that $\boldsymbol{m}_t^2=N$ that is perpendicular to $\boldsymbol{e}$: $\boldsymbol{e}\cdot\boldsymbol{m}_t=0$. Thus, the coefficient a_ℓ represents here the ratio between standard deviation and average of the components t_i.

Given the existence of this self-stress, we are interested in the minimal possible average length $\bar{\ell}$ for fixed σ_ℓ.

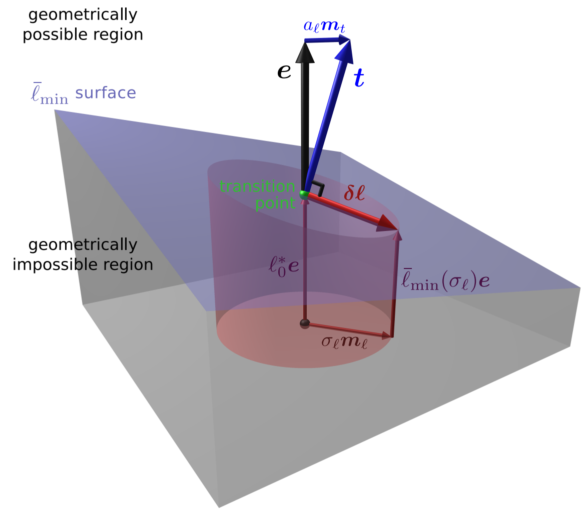

FIG. S1. Schematic illustrating the relation between the minimal length $\bar{\ell}_{\min}$ hyper-surface (blue surface) and the self-stress $\boldsymbol{t}$ (thick blue arrow) that is created at the onset of geometric incompatibility. Here, we show a 3D representation of the N-dimensional hyperspace containing all rescaled spring lengths $\boldsymbol{\ell}=(\ell_1,\dots,\ell_N)$. The space is rotated such that the axis pointing up corresponds to the average spring length, i.e. it is parallel to the vector $\boldsymbol{e}=(1,\dots,1)$ (black arrow). The horizontal plane in the image represents the remaining $N-1$ dimensions in the $\boldsymbol{\ell}$ space. The blue $\bar{\ell}_{\min}$ surface separates a geometrically possible region above it from a region of geometrically impossible spring length combinations $\boldsymbol{\ell}$ below it. Setting the spring rest lengths to the latter combinations will thus lead to geometric incompatibility and thus potentially rigidify the network. Close to the transition point (green sphere), the $\bar{\ell}_{\min}$ surface is perpendicular to the self-stress $\boldsymbol{t}$ (blue arrow), as expressed by Eq. (S18). The black sphere marks the point where all spring lengths are zero, and at the transition point (green sphere), all springs attain the same length $\boldsymbol{\ell}=\ell_0^*\boldsymbol{e}$. The distance from the line connecting both black and green points corresponds to the standard deviation of the spring lengths σ_ℓ (with a prefactor of $\sqrt{N}$). Hence, to obtain the minimal average length $\bar{\ell}_{\min}$ for given σ_ℓ, we need to cut the mantle of a cylinder with radius $\sqrt{N}\sigma_\ell$ (red cylinder) with the $\bar{\ell}_{\min}$ surface. As we show via Eq. (S19), the resulting ellipse has its lowest point where $\boldsymbol{m}_\ell\uparrow\uparrow\boldsymbol{m}_t$. This figure corresponds to the case without area term. Also, this discussion relates to a local environment of one transition point. We expect that large displacements of the degrees of freedom $\boldsymbol{r}$ will affect this diagram by changing the direction of $\boldsymbol{m}_t$ (and by slightly altering the values of ℓ_0^* and a_ℓ).

Similar to $\boldsymbol{t}$, we express the vector $\boldsymbol{\ell}$ containing all spring lengths as:

$$\boldsymbol{\ell}=\bar{\ell}\boldsymbol{e}+\sigma_\ell\boldsymbol{m}_\ell, \tag{S16}$$

where again $\boldsymbol{m}_\ell$ is a vector perpendicular to $\boldsymbol{e}$ normalized such that $\boldsymbol{m}_\ell^2=N$. Right at the transition point $\ell_0=\ell_0^*$, all lengths attain their preferred value $\boldsymbol{\ell}=\ell_0^*\boldsymbol{e}$. As we slightly decrease the control parameter ℓ_0 by $\delta\ell_0$, and thus move into the rigid regime, the degrees of freedom will change by $\boldsymbol{\delta r}$. To first order in $\delta\ell_0$ this creates a change in $\boldsymbol{\ell}$ by

$$\boldsymbol{\delta\ell} = \boldsymbol{C} \cdot \boldsymbol{\delta r}, \tag{S17}$$

where $\boldsymbol{\delta\ell} = (\bar{\ell} - \ell_0^*)\boldsymbol{e} + \sigma_\ell \boldsymbol{m}_\ell$. To minimize $\bar{\ell}$ for fixed σ_ℓ, we need to take into account that $\boldsymbol{\delta\ell}$ can not attain any vector in its N-dimensional vector space. In particular, the existence of the self-stress $\boldsymbol{t}$ implies that $\boldsymbol{\delta\ell}$ has to be perpendicular to $\boldsymbol{t}$ (using Eqs. (S14) and (S17)):

$$\boldsymbol{t} \cdot \boldsymbol{\delta\ell} = 0. \tag{S18}$$

This equation is essentially a linearized version of the geometric compatibility condition $\bar{\ell} \geq \bar{\ell}_{\min}(\sigma_\ell)$. Note that Eq. (S18) is the only constraint when minimizing $\bar{\ell}$, besides fixing σ_ℓ, because $\boldsymbol{t}$ is the only self-stress. Inserting Eq. (S15) and $\boldsymbol{\delta\ell}$ into Eq. (S18) yields:

$$\bar{\ell} = \ell_0^* - a_\ell \sigma_\ell (\boldsymbol{m}_t \cdot \boldsymbol{m}_\ell / N). \tag{S19}$$

The minimal $\bar{\ell}$ is obtained for $\boldsymbol{m}_\ell = \boldsymbol{m}_t$, where the scalar product $\boldsymbol{m}_t \cdot \boldsymbol{m}_\ell$ attains its maximal possible value N. Thus:

$$\bar{\ell}_{\min}(\sigma_\ell) = \ell_0^* - a_\ell \sigma_\ell. \tag{S20}$$

Insertion into Eq. (S16) yields:

$$\boldsymbol{\ell}(\sigma_\ell) = (\ell_0^* - a_\ell \sigma_\ell)\boldsymbol{e} + \sigma_\ell \boldsymbol{m}_t. \tag{S21}$$

Hence, also each individual spring length depends linearly on σ_ℓ.

This proof is schematically illustrated by Fig. S1, where the N-dimensional space of spring lengths $\boldsymbol{\ell}$ is represented by a 3D figure. As for Eq. (S18), the $\bar{\ell}_{\min}$ surface (blue surface) is locally perpendicular to the self-stress $\boldsymbol{t}$ (blue arrow). In order to find the minimal possible $\bar{\ell}$ for given standard deviation σ_ℓ, we first cut the $\bar{\ell}_{\min}$ surface with the locus where the standard deviation σ_ℓ has a defined constant value, which is a cylinder mantle (red). The cut is an ellipse, and as we show through Eq. (S19), its lowest point is where $\boldsymbol{m}_\ell \upuparrows \boldsymbol{m}_t$. Because the radius of the cylinder is proportional to σ_ℓ, and because the blue $\bar{\ell}_{\min}$ surface is locally linear, we obtain that indeed $\ell_0^* - \bar{\ell}_{\min}(\sigma_\ell) \sim \sigma_\ell$.

To take heterogeneities in the weights w_i into account, one can completely follow the above line of argument, where only the formal definition of the scalar product in the N-dimensional "constraint space" needs to be changed. In particular, the scalar product between two N-dimensional vectors $\boldsymbol{p}$ and $\boldsymbol{q}$ needs to be defined as:

$$\boldsymbol{p} \cdot \boldsymbol{q} = \sum_i w_i p_i q_i. \tag{S22}$$

Consequentially, also averages and standard deviations change, e.g. $\bar{t} = \boldsymbol{e} \cdot \boldsymbol{t}/N = [\sum_i w_i t_i]/N$ and $\sigma_t^2 = (\boldsymbol{t} - \bar{t}\boldsymbol{e})^2/N = [\sum_i w_i (t_i - \bar{t})^2]/N$.

For the cellular models with area term, the line of argument is similar, but with the following changes: First, vectors in the "constraint space" like the self-stress $\boldsymbol{t}$ now contain $2N$ components (where N is the number of cells): N of these components represent cell "lengths" and the other N components represent cell "areas". Second, because the overall area is constant, there is a second self-stress where the length components are zero and the area components are one: $(0, \ldots, 0, 1, \ldots, 1)$. However, the important self-stress is still $\boldsymbol{t}$, which is now written as $\boldsymbol{t} = \boldsymbol{e} + a_\ell \boldsymbol{m}_t^\ell + a_a \boldsymbol{m}_t^a$, where $\boldsymbol{e} = (1, \ldots, 1, 0, \ldots, 0)$, the vector $\boldsymbol{m}_t^\ell$ has only non-zero length entries, and the vector $\boldsymbol{m}_t^a$ has only non-zero area entries. Consequentially, minimization of $\bar{\ell}$ for fixed σ_ℓ and σ_a yields: $\bar{\ell}_{\min}(\sigma_\ell, \sigma_a) = \ell_0^* - a_\ell \sigma_\ell - a_a \sigma_a$.

Here we have assumed that at at the transition point $\ell_0 = \ell_0^*$, all spring lengths attain their preferred value $\ell_i = \ell_0^*$. In Section II A we numerically show that this is the case is nearly all of our models. However, it is in principle possible that this is not the case, but only if there are prestresses in the floppy regime, which we occasionally observed for the 2D vertex model with $k_A > 0$ (Fig. S4) and the 3D Voronoi model with $k_V > 0$ [2]. While we consider these exceptions outside the scope of the current paper, the above derivation can easily be generalized to obtain a formula for $\bar{\ell}_{\min}$ that includes these cases.

C. Geometric properties and energy

Here we show how for all studied models, the function $\bar{\ell}_{\min}(\sigma_\ell, \sigma_a, \gamma)$ controls the behavior of the system in the rigid regime. In particular, knowing the functional form of $\bar{\ell}_{\min}(\sigma_\ell, \sigma_a, \gamma)$ lets us write explicit expressions for $\bar{\ell}$, σ_ℓ, σ_a, and the total system energy e in terms of the control parameters k_A, ℓ_0, and γ.

1. *Without shear strain*

For all models, the dimensionless system energy e can be expressed in terms of $\bar{\ell}$, σ_ℓ, and σ_a:

$$e = N\Big[(\bar{\ell} - \ell_0)^2 + \sigma_\ell^2 + k_A \sigma_a^2\Big]. \tag{S23}$$

Because in the rigid regime, the average length attains the minimally possible length given σ_ℓ and σ_a, the energy minimum fulfills the following two equations:

$$0 = \frac{\partial e\Big(\bar{\ell} = \bar{\ell}_{\min}(\sigma_\ell, \sigma_a), \sigma_\ell, \sigma_a\Big)}{\partial \sigma_\ell} \tag{S24}$$

$$0 = \frac{\partial e\Big(\bar{\ell} = \bar{\ell}_{\min}(\sigma_\ell, \sigma_a), \sigma_\ell, \sigma_a\Big)}{\partial \sigma_a}. \tag{S25}$$

Insertion of Eq. (S23) yields:

$$\sigma_\ell = -\frac{\partial \bar{\ell}_{\min}}{\partial \sigma_\ell}(\bar{\ell} - \ell_0) \tag{S26}$$

$$\sigma_a = -\frac{1}{k_A}\frac{\partial \bar{\ell}_{\min}}{\partial \sigma_a}(\bar{\ell} - \ell_0). \tag{S27}$$

If we knew the relation $\bar{\ell}_{\min}(\sigma_\ell, \sigma_a)$, we could just insert it together with $\bar{\ell} = \bar{\ell}_{\min}$ into Eqs. (S26) and (S27) in order to obtain explicit expressions for $\bar{\ell}$, σ_ℓ, and σ_a depending on the control parameters ℓ_0 and k_A.

For example, close to the transition point we find that $\bar{\ell}_{\min}(\sigma_\ell, \sigma_a)$ depends linearly on σ_ℓ and σ_a:

$$\bar{\ell}_{\min}(\sigma_\ell, \sigma_a) = \ell_0^* - a_\ell \sigma_\ell - a_a \sigma_a. \tag{S28}$$

This is a consequence of the self-stress that is created at the onset of rigidity (see Section I B). Insertion into Eqs. (S26) and (S27) yields:

$$\sigma_\ell = a_\ell(\bar{\ell} - \ell_0) \tag{S29}$$

$$\sigma_a = \frac{a_a}{k_A}(\bar{\ell} - \ell_0). \tag{S30}$$

Further, using again Eq. (S28), we obtain:

$$\bar{\ell} = \ell_0 + \frac{1}{Z}(\ell_0^* - \ell_0) \tag{S31}$$

$$\sigma_\ell = \frac{a_\ell}{Z}(\ell_0^* - \ell_0) \tag{S32}$$

$$\sigma_a = \frac{a_a}{k_A Z}(\ell_0^* - \ell_0) \tag{S33}$$

with

$$Z = 1 + a_\ell^2 + \begin{cases} 0 & \text{for } k_A = 0, \text{ and} \\ \frac{a_a^2}{k_A} & \text{for } k_A > 0. \end{cases} \tag{S34}$$

Finally, inserting Eqs. (S31)–(S33) into Eq. (S23), we obtain an explicit expression of e in terms of the control parameters ℓ_0 and k_A:

$$e = \frac{N}{Z}(\ell_0^* - \ell_0)^2, \tag{S35}$$

where Z depends on k_A according to Eq. (S34).

2. *Including shear strain*

The minimal length function generally depends also on the shear strain γ. Note that in our formalism there are no requirements on the precise definition of γ, which can in particular describe any of both pure shear or simple shear deformation. Please refer to Section IV for the precise definition of γ used in each of the studied models.

We assume that $\bar{\ell}_{\min}(\sigma_\ell, \sigma_a, \gamma)$ is analytic in γ, and close to the transition, we can thus write up to first order in σ_ℓ and σ_a and up to second order in γ:

$$\bar{\ell}_{\min}(\sigma_\ell, \sigma_a, \gamma) = \ell_0^* - a_\ell \sigma_\ell - a_a \sigma_a + b\gamma^2. \tag{S36}$$

Note that there is some freedom in choosing the point $\gamma = 0$, which allows us to discard the linear term $\sim \gamma$ in Eq. (S36). This point is automatically reached by searching for the point $\ell_0 = \ell_0^*$ and $\gamma = 0$ using a shear-stabilized minimization protocol for simulations [3], or in experiments by starting from a stress-free state with minimal ℓ_0 (Section I D). Moreover, generally there are of course also terms $\sim \sigma_{\ell/a}\gamma$ and $\sim \sigma_{\ell/a}\gamma^2$. These terms allow to predict higher-order corrections to the energy and its derivatives. However, for this study we focus just on the highest-order terms as listed in Eq. (S36).

Following the same arguments as in the previous subsection, we ultimately obtain for the system energy:

$$e = \frac{N}{Z}\left(\ell_0^* - \ell_0 + b\gamma^2\right)^2, \tag{S37}$$

where Z is again given by Eq. (S34). In the following Sections I D and I E below we compute several derivatives of this expression to obtain the mechanical material properties.

D. Shear stress and shear modulus

Using the expression Eq. (S37), we obtain the following expression for the shear stress $\tilde{\sigma} = (\mathrm{d}e/\mathrm{d}\gamma)/N$ in the rigid regime, with N being the dimensionless system area:

$$\tilde{\sigma} = \frac{4b\gamma}{Z}\left(\ell_0^* - \ell_0 + b\gamma^2\right). \tag{S38}$$

Note that a term $\sim \gamma$ in $\ell_{\min}$ (Eq. (S36)) would lead to an additional constant term in the numerator of Eq. (S38). Thus, the shear stress for $\ell_0 < \ell_0^*$ would be nonzero at $\gamma = 0$.

From Eq. (S38), we obtain the differential shear modulus $G = \mathrm{d}\tilde{\sigma}/\mathrm{d}\gamma$ in the rigid regime:

$$G = \frac{4b}{Z}\left(\ell_0^* - \ell_0 + 3b\gamma^2\right). \tag{S39}$$

Combining this with Eq. (S38), we obtain:

$$G = \Delta G^* + \frac{3\tilde{\sigma}}{\gamma}, \tag{S40}$$

where ΔG^* is:

$$\Delta G^* = \frac{8b}{Z}(\ell_0 - \ell_0^*). \tag{S41}$$

This is the shear modulus discontinuity in G, which appears at the onset of rigidity $\gamma = \gamma^*$.

For $\gamma = 0$ and $\ell_0 < \ell_0^*$, Eq. (S39) implies that the shear modulus G scales linearly with the distance $\ell_0^* - \ell_0$ to the transition point. This is confirmed by our model simulations for the 2D spring networks in Fig. 4f in the main text, and for the cellular models in Fig. S2, in part confirming earlier findings [2, 4, 5]. Fig. S2 also shows a collapse of the different $k_A > 0$ curves of a given model when rescaling the shear modulus with Z, indicating that b indeed describes the underlying geometry and is thus independent of k_A. However, note that like the coefficients a_ℓ, also the coefficient b may differ between the $k_A = 0$ and $k_A > 0$ versions of a model (see in particular

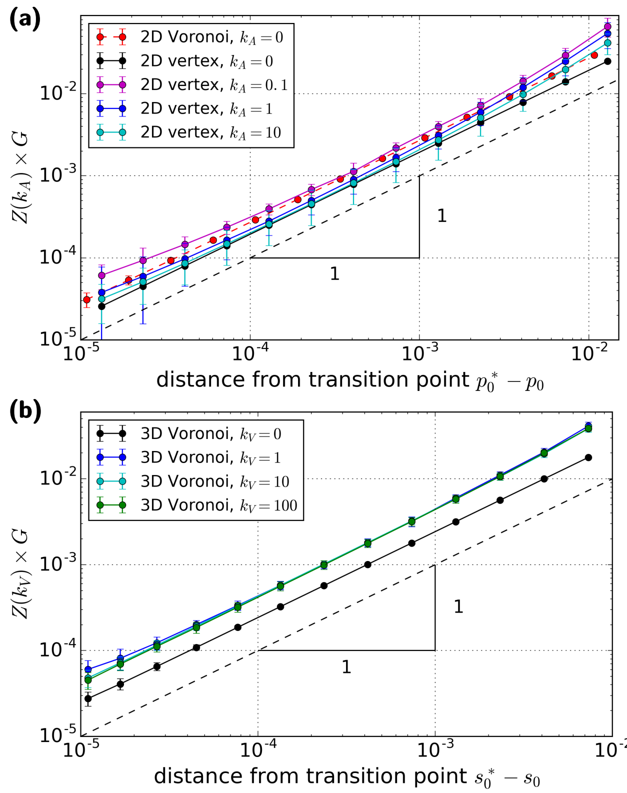

FIG. S2. For $\gamma = 0$ and $\ell_0 < \ell_0^*$, the shear modulus G scales linearly with the distance $\ell_0^* - \ell_0$ to the transition point (cf. Eq. (S39)). (a) 2D Voronoi and 2D vertex model, (b) 3D Voronoi model. Rescaling the shear modulus by Z defined in Eq. (S34) largely collapses the data for all $k_A > 0$ values of a given model.

Fig. S2b). The reason is that they represent Taylor expansions of the function $\bar{\ell}_{\min}(\sigma_\ell, \sigma_a, \gamma)$ at different points $(\sigma_\ell, \sigma_a, \gamma)$. For $k_A > 0$, the coefficient b characterizes the behavior at $(\sigma_\ell, \sigma_a, \gamma) = (0, 0, 0)$, while for $k_A = 0$ at $(\sigma_\ell, \sigma_a, \gamma) = (0, \sigma_a > 0, 0)$. The numerical values of b are noted in Table I in the main text.

E. Isotropic stress and bulk modulus

In order to derive the isotropic part of the stress and the bulk modulus from the energy expression Eq. (S37), we make use of the fact that ℓ_0 is non-dimensionalized by the number density of elements, and thus indirectly depends on the system size.

To make sure we are not missing any term, we start from the "dimensionful" energy of the system, which reads:

$$E = \sum_i \Big[K_L(L_i - L_0)^2 + K_A(A_i - A_0)^2\Big]. \tag{S42}$$

Here, K_L and K_A are length and area rigidities, L_i and A_i are length and area of element i, and L_0 and A_0 are their respective preferred values. Thus, the total area of the system is $A_T = \sum_i A_i$ and the average area per element is $\bar{A} = A_T/N$. To obtain the dimensionless expressions e for the energies of our models (Eqs. (1)–(4) in the main text), we have set $A_0 = \bar{A}$ and then non-dimensionalized with respect to the length scale $\bar{A}^{1/D}$ and the energy scale $K_L\bar{A}^{2d/D}$ [2, 6, 7]. Hence, the dimensionful total energy E of the system can be written as the sum:

$$E = E_{A_0} + K_L\bar{A}^{2d/D}e, \tag{S43}$$

where $E_{A_0} = NK_A(\bar{A} - A_0)^2$ is a mean-field contribution by the area elasticity, and e is the non-dimensional energy given by Eq. (S37).

The isotropic part of the stress is defined as the negative (dimensionful) pressure $-P = \mathrm{d}E/\mathrm{d}A_T = (\mathrm{d}E/\mathrm{d}\bar{A})/N$. Insertion of Eq. (S43) yields:

$$-P = 2K_A(\bar{A} - A_0) + \frac{K_L\bar{A}^{2d/D}}{N}\left[\frac{2d}{D\bar{A}}e + \frac{\mathrm{d}e}{\mathrm{d}\bar{A}}\right]. \tag{S44}$$

We obtain for the dimensionless pressure $p = \bar{A}^{1-2d/D}P/K_L$:

$$-p = 2k_A(1 - a_0) + \frac{1}{N}\left[\frac{2d}{D}e + \bar{A}\frac{\mathrm{d}e}{\mathrm{d}\bar{A}}\right] \tag{S45}$$

with $a_0 = A_0/\bar{A}$.

While in the floppy regime the dimensionless energy e is zero, in the rigid regime e is given by Eq. (S37) in terms of shear strain γ and the dimensionless control parameters $k_A = K_A\bar{A}^{2-2d/D}/K_L$ and $\ell_0 = L_0/\bar{A}^{d/D}$. The derivatives of k_A and ℓ_0 with respect to $\bar{A}$ are:

$$\frac{\mathrm{d}k_A}{\mathrm{d}\bar{A}} = \frac{2(D-d)k_A}{D\bar{A}} \qquad \frac{\mathrm{d}\ell_0}{\mathrm{d}\bar{A}} = -\frac{d\ell_0}{D\bar{A}}. \tag{S46}$$

Hence, we ultimately obtain for the pressure p to first order in $\ell_0^* - \ell_0 + b\gamma^2$ and for $b\gamma^2 \ll \ell_0^*$:

$$-p = 2k_A(1 - a_0) + \frac{2d\ell_0^*}{DZ}(\ell_0^* - \ell_0 + b\gamma^2). \tag{S47}$$

Comparison with the shear modulus G, Eq. (S39), for $k_A = 0$ or $a_0 = 1$ yields the second relation in Eq. (13) in the main text.

From Eq. (S47) directly follows that the Poynting coefficient $\chi = p/\gamma^2$ close to $\ell_0 = \ell_0^*$ is for $k_A = 0$ or $a_0 = 1$:

$$\chi = -\frac{2db\ell_0^*}{DZ}. \tag{S48}$$

For 2D spring networks, this prediction is tested in Fig. S5b & inset.

The bulk modulus is defined by $-A_T(\mathrm{d}P/\mathrm{d}A_T) = -\bar{A}(\mathrm{d}P/\mathrm{d}\bar{A})$, and thus the dimensionless bulk modulus is

$$B = -\frac{\bar{A}^{2-2d/D}}{K_L}\frac{\mathrm{d}P}{\mathrm{d}\bar{A}}. \tag{S49}$$

Insertion of the pressure P, Eq. (S44), yields in the floppy regime:

$$B = 2k_A, \tag{S50}$$

and in the rigid regime:

$$B = 2k_A + \frac{1}{N}\left[\frac{2d(2d-D)}{D^2}e + \frac{4d}{D}\bar{A}\frac{\mathrm{d}e}{\mathrm{d}\bar{A}} + \bar{A}^2\frac{\mathrm{d}^2 e}{\mathrm{d}\bar{A}^2}\right]. \tag{S51}$$

To absolute order in $\ell_0^* - \ell_0 + b\gamma^2$ and for $\gamma = 0$, only the last term in the square brackets survives when inserting Eq. (S37):

$$B = 2k_A + \frac{2d^2(\ell_0^*)^2}{D^2 Z}. \tag{S52}$$

This is the bulk modulus when approaching the transition from the rigid regime. To extend this expression for $\gamma \neq 0$ and into the rigid regime $\ell_0^* - \ell_0 + b\gamma^2 > 0$, higher order terms in $\bar{\ell}_{\mathrm{min}}$ need to be taken into account. Note that Eq. (S52) can also be derived by projecting the affine isotropic deformation mode onto the self-stress $\boldsymbol{t}$ that is created at the onset of geometric incompatibility (Section I B) [1].

The prefactor Z in Eq. (S52), and thus ultimately the coefficients a_ℓ and a_a (Eq. (S34)), represent the effect of non-affinities during isotropic deformations. To see this, consider a system at the transition point, where all dimensionless areas are $a_i = 1$ and all dimensionless lengths are $\ell_i = \ell_0^*$. An *affine* isotropic deformation starting from this configuration means that all dimensionless a_i and ℓ_i stay the same, because we non-dimensionalize with the average area $\bar{A}$. With Eq. (S23) follows that the energy for affine transformations away from the transition point towards the solid regime would then be $e = N(\ell_0^* - \ell_0)^2$. The difference to Eq. (S37) is just the prefactor Z^{-1}, which thus indeed accounts for the non-affinities.

F. Scaling exponents for 2D spring networks

Here we rationalize for the 2D spring networks the observed approximate scaling exponents in the coefficients $a_\ell \sim \Delta z^{1/2}$ (Fig. 2a inset in the main text) and $b \sim \Delta z$ (Fig. 4c inset in the main text).

To understand the scaling of the coefficient a_ℓ, we start with the extended Hessian $\boldsymbol{H}_\lambda$ of the system, which we define as the second energy derivative with respect to both, all internal degrees of freedom r_n *and a global linear scaling factor* λ. We denote the eigen frequencies of this extended Hessian by $(\omega_\lambda^m)^2$ and the λ component of the corresponding eigen vectors by Λ_λ^m. Then, the bulk modulus $B = (\mathrm{d}^2E/\mathrm{d}\lambda^2)/D^2N$ can be expressed using the well-known formula [2, 8, 9]:

$$\left[\frac{\mathrm{d}^2 E}{\mathrm{d}\lambda^2}\right]^{-1} = \sum_m \frac{(\Lambda_\lambda^m)^2}{(\omega_\lambda^m)^2}. \tag{S53}$$

We use this formula in the rigid regime approaching the transition. In this case, there are many low-frequency modes, which correspond to the zero modes in the floppy regime. However, as evidenced by the bulk modulus discontinuity, these modes have vanishing λ component [1, 2]: $\Lambda_\lambda^m = 0$. Thus, we can treat the quantities on the right-hand side of Eq. (S53) as those of the unstressed Hessian, ignoring any zero modes in the sum [2]. Insertion of Eq. (S52) and transforming the sum into an integral yields:

$$1 + a_\ell^2 \sim \int_{0+}^{\infty} \frac{D_\lambda(\omega)\Lambda_\lambda^2(\omega)}{\omega^2}\,\mathrm{d}\omega. \tag{S54}$$

Here $D_\lambda(\omega)$ is the density of states, and we used that ℓ_0^* is to dominant order independent of Δz (Table I and Fig. 1b inset in main text). It has been shown that for the "non-extended" Hessian $\boldsymbol{H}$, the density of states D shows a plateau starting at $\omega^* \sim \Delta z$ [10, 11]. Assuming that Λ_λ does not depend strongly on ω and that $D_\lambda \simeq D$, we obtain

$$1 + a_\ell^2 \sim \frac{1}{\Delta z}. \tag{S55}$$

For $\Delta z \ll 1$ follows indeed that $a_\ell \sim \Delta z^{1/2}$. Deviations that we observe in our 2D system for small Δz (Fig. 2a inset in the main text) may be related to logarithmic corrections [11].

We use a related argument to understand the scaling of the coefficient b. Now we use the Hessian $\boldsymbol{H}_\gamma$ extended by the shear strain γ. Analogously to above, we denote the eigen frequencies of this extended Hessian by $(\omega_\gamma^m)^2$ and the γ component of the corresponding eigen vectors by Λ_γ^m. We use the analogous formula to Eq. (S53) for the shear modulus [2, 8, 9]:

$$\frac{1}{NG} = \sum_m \frac{(\Lambda_\gamma^m)^2}{(\omega_\gamma^m)^2}. \tag{S56}$$

Using Eqs. (S39) and (S47) with $\gamma = 0$, this equation can be transformed into

$$\frac{1}{b(-p)} \sim \int_{0+}^{\infty} \frac{D_\gamma(\omega)\Lambda_\gamma^2(\omega)}{\omega^2}\,\mathrm{d}\omega. \tag{S57}$$

Here, $-p$ is the isotropic stress acting on the boundaries of the system. The major difference to the isotropic case, Eq. (S54), is that the shear modulus *vanishes* when approaching the point $\ell_0 = \ell_0^*$ and $\gamma = 0$ from the rigid side. This means that right at the transition, there are zero modes of D_γ with non-vanishing overlap $\Lambda_\gamma^m \neq 0$. As a consequence, in the rigid vicinity of the transition where $-p$ is small, the integral Eq. (S57) is dominated by these modes, which are raised to energies $\sim (-p)$ [2]. Indeed, some of us recently showed that for small $-p$, the product $D_\gamma\Lambda_\gamma^2$ collapses for different Δz and $-p$ as [12]:

$$D_\gamma(\omega)\Lambda_\gamma^2(\omega)\,\mathrm{d}\omega = \Delta z f_\gamma(x)\,\mathrm{d}x \tag{S58}$$

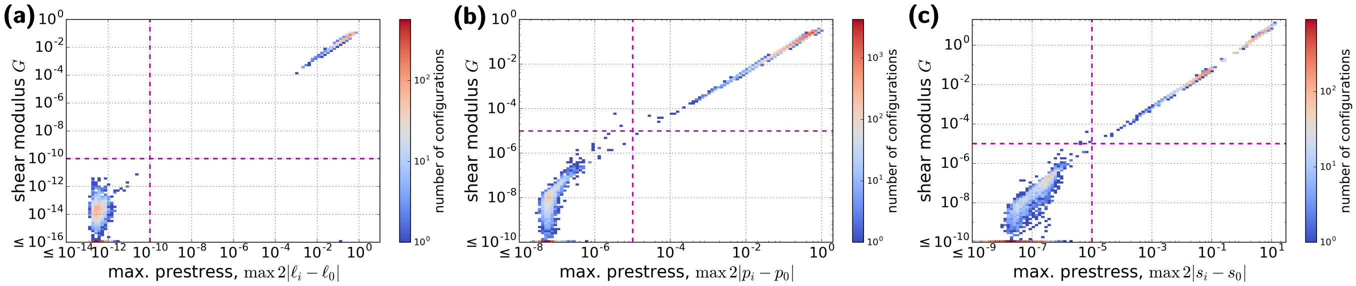

FIG. S3. Rigidity is created by geometric incompatibility. This is shown here by 2D histograms with respect to the largest prestress in a given configuration (directly indicating geometric incompatibility, x axis) and its shear modulus (y axis), for (a) 2D spring networks, here with $z = 3.2$, (b) the 2D vertex model with $k_A = 0$ and (c) the 3D Voronoi model with $k_V = 0$. Earlier publications have shown this for the 2D Voronoi model with $k_A = 0$ [7] and the 3D Voronoi model with $k_V > 0$ [2].

with $x = \omega/\sqrt{-p}$ and f_γ being independent of Δz and p. This makes sense, because at the transition there are $\sim \Delta z$ zero modes, which are all raised to energies $\sim (-p)$. Insertion of Eq. (S58) into Eq. (S57) yields:

$$\frac{1}{b(-p)} \sim \frac{\Delta z}{-p}, \tag{S59}$$

and thus $b \sim 1/\Delta z$. More details on the shear modulus scaling in the spring networks can be found in Ref. [12].

G. Application to rheometer geometry

To facilitate the comparison of our results to experiments, we briefly discuss here how our results apply to a rheometer geometry with circumferential axis x, radial axis y, and rotation axis z, and the shear strain γ corresponds to the simple shear strain. Rheometers typically measure shear stress $\tilde{\sigma} = \sigma_{xz}$ and normal stress σ_{zz}.

In the following, we show for that several experimental protocols, and in the vicinity of the $(\gamma, \ell_0) = (0, \ell_0^*)$ point, the normal stress σ_{zz} should be dominated by the isotropic part of the stress tensor, $-p$, given by Eq. (S47). To this end, we will assume no lateral (i.e. radial) deformation of the network in the rheometer, which we expect to be valid whenever the sample is glued to the rheometer plates and its height is small as compared to its radius.

First, we expect the normal stress σ_{zz} to be dominated by the isotropic stress, $\sigma_{zz} \simeq -p$, upon application of simple shear starting from a stress-free state. To show this, we use the Lodge-Meissner relation [13], which states that the normal stress difference is:

$$\sigma_{xx} - \sigma_{zz} = \tilde{\sigma}\gamma. \tag{S60}$$

Note that while this relation likely holds generally for isotropic, purely elastic materials, we consider a proof of this to be outside the scope of this article. Combined with Eqs. (S38) and (S47), we find:

$$\sigma_{xx} - \sigma_{zz} = -\frac{2Db\gamma^2}{d\ell_0^*}p. \tag{S61}$$

Hence, for $\gamma \ll 1$ we obtain that the normal stress difference is much smaller than the isotropic stress $-p$, and thus $\sigma_{zz} \simeq -p$.

We expect the same also for uniaxial compression or expansion of the sample along the z axis [14]. This is because in the absence of lateral deformation, both isotropic strain and pure shear strain along the z axis will have the same magnitude ε. When expanding the sample starting from $\ell_0 = \ell_0^*$, the discontinuity in the bulk modulus will lead to lowest order in ε to a linear increase in the isotropic stress $-p \sim \varepsilon$. However, because of the linear increase of the shear modulus with $(\ell_0^* - \ell_0) \sim \varepsilon$, the normal stress difference will increase only as $\sim \varepsilon^2$. Hence, we find also for small uniaxial deformations: $\sigma_{zz} \simeq -p$.

II. NUMERICAL RESULTS

A. Rigidity is created by geometric incompatibility

Here we discuss numerical evidence showing that geometric incompatibility is both necessary and sufficient to create rigidity in the models studied. We have shown this before for the $k_V > 0$ case of the 3D Voronoi model [2] and for the $k_A = 0$ case for the 2D Voronoi model [7]. For the 2D spring networks, the 2D vertex model with $k_A = 0$, and the 3D Voronoi model with $k_V = 0$, we demonstrate this in Fig. S3.

In Fig. S3, we sorted all energy-minimized configurations into two-dimensional histograms with respect to the shear modulus G and the maximal prestress $2|\ell_i - \ell_0|$ in the configuration. The dashed magenta lines indicate cutoff values below which we regard shear modulus and maximal prestress as numerically zero (obtained as described in [2]). The fact that the upper-left and lower-right quadrants in all three plots are essentially devoid of configurations means that geometric incompatibility is necessary and sufficient, respectively, to create rigidity in these models.

For the 2D vertex model with $k_A > 0$ we find exceptions to this, similar to the 3D Voronoi model with $k_V > 0$ [2]. Note that all results presented here are

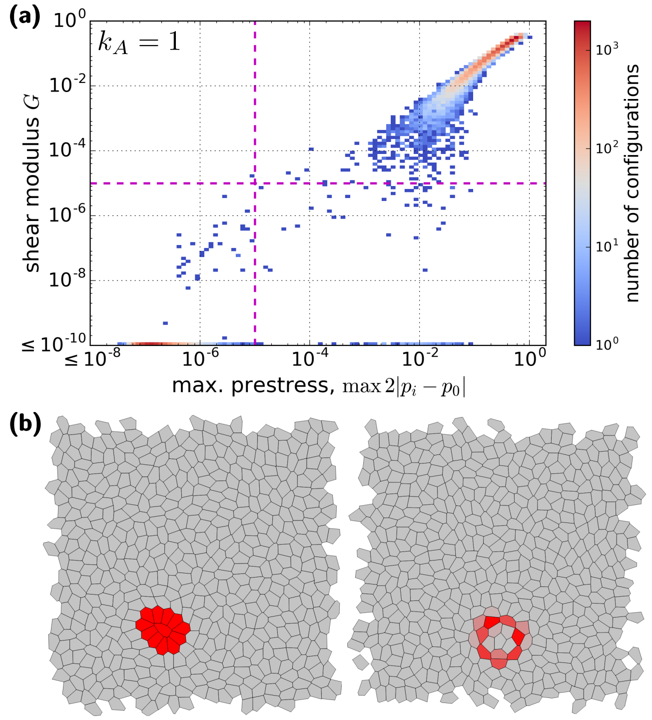

FIG. S4. In the 2D vertex model with $k_A > 0$, rigidity is created by the onset of geometric incompatibility, but there are also localized prestresses. (a) Geometric incompatibility is necessary for rigidity, and in many cases also sufficient. However, there were several energy-minimized configurations with finite prestresses, but vanishing shear modulus. (b) Two such configurations, with $p_0 = 3.939$ and $p_0 = 3.939$, respectively. The color of each cell i indicates $p_i - p_0$, where gray corresponds to a value of zero and bright red to a value of 0.05. $k_A = 1$ in both panels. Shown here are only configurations without quadrilaterals (see Section IV).

based on configurations without quadrilaterals and triangles (see Section IV). Like for the other models, also for the 2D vertex model with $k_A > 0$ geometric incompatibility (i.e. the existence of prestresses) is *necessary* to create rigidity (i.e. a finite shear modulus). This is suggested by the essential absence of configurations in the upper-left quadrant in Fig. S4a. However, the existence of prestresses is not always *sufficient* to rigidify the system, as can be seen by the configurations in the lower-right quadrant of this plot. Examples for such configurations are shown in Fig. S4b, where the color indicates the value of $p_i - p_0$ of each cell, with gray indicating a value of zero and red indicating a positive value. The cells with finite perimeter tension are localized to one region and do not percolate the system. Note that when probing the scaling of $\ell_{\min}$ and of mechanical properties, we excluded networks with such localized prestresses (i.e. in Fig. 2b in the main text, Fig. S2a, and Fig. S7d-f).

B. 2D spring networks

Here we report additional numerical results on the 2D spring networks. First, we found occasional jumps when probing the dependence of the critical shear strain γ^* on $\ell_0 > \ell_0^*$ (see Fig. S5a for $z = 3.7$). We observed that these jumps occur more frequently for higher coordination number z, i.e. for systems closer to isostaticity. We interpret these jumps as plastic events where the system switches into the basin of a different minimum of $\ell_{\min}(0, \gamma)$. In particular, we numerically looked for the critical strain γ^* by increasing γ in steps of size $\Delta\gamma$ until the system rigidified (see Section IV). Notably, upon decreasing $\Delta\gamma$, we obtained less jumps in γ^*, consistent with a decreased probability of switching basins when taking smaller steps. Throughout this article, we focus on the purely elastic behavior of the system in the vicinity of one local minimum of $\bar{\ell}_{\min}(\sigma_\ell = 0, \gamma)$, and exclude these cases from our analysis.

Second, in the past, randomly-cut packing-derived spring networks have been studied without varying the parameter ℓ_0, where instead the value ℓ_0^{init} right after initialization of the spring network was used, e.g. in Ref. [15]. In order to compare to the scaling relations with respect to Δz found in the past, we numerically studied the scaling of $\ell_0^{\text{init}} - \ell_0^*$ and find that it scales as $(\ell_0^{\text{init}} - \ell_0^*) \sim \Delta z$. Together with our other findings, we recapitulate indeed several of the scaling exponents observed in Ref. [15] (see discussion section in the main text).

Third, we also observe a negative Poynting effect, which is reflected in the development of a tensile isotropic stress $-p$ upon shear. For $\ell_0 = \ell_0^*$, the isotropic stress scales quadratically with the shear strain γ, which is shown in Fig. S5b for $z = 3.2$. Moreover, we can predict the corresponding coefficient $\chi = p/\gamma^2$ using Eq. (S48) by extracting the coefficient b for each network from the scaling of the critical shear γ^* with $\ell_0 > \ell_0^*$ (Fig. S5b inset).

Fourth, the existence of the function $\ell_{\min}$ allows the prediction not only of the Poynting coefficient χ, but also of the coefficient describing the linear shear modulus scaling for $\ell_0 < \ell_0^*$ (Fig. S5c, cf. Fig. 4f) and of the shear modulus discontinuity (Fig. S5c inset, cf. Fig. 4d inset).

C. 2D fiber networks without bending rigidity

We also simulated a fiber network model without bending rigidity. To this end, we divided each spring of our 2D spring networks into M “subsprings” (Fig. S6a). These subspring networks are still under-constrained, and the limit $M \to \infty$ corresponds to fiber networks without bending rigidity. We find that such subspring networks also follow the predictions that we make in the main text (Fig. S6b-e, cf. Fig. 4 in the main text). Moreover, we also find numerically that these results are quantita-

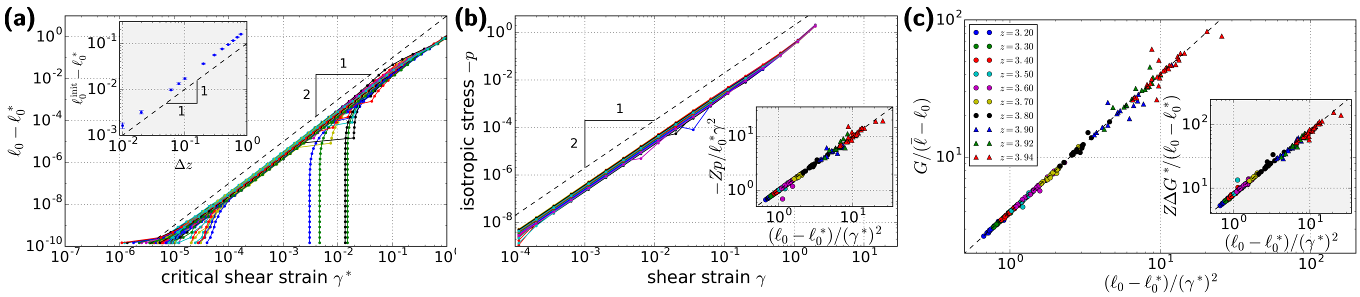

FIG. S5. Additional numerical results for the scaling in 2D spring networks. (a) Dependence of the critical shear γ^* on $\ell_0 - \ell_0^*$ for $z = 3.7$ (cf. Fig. 4c in the main text). We interpret the jumps in γ^* as a switch of the system into the basin of a different minimum of $\ell_{\min}(0, \gamma)$. (a inset) The value of ℓ_0 right after creation of the spring network, ℓ_0^{init}, behaves such that we numerically observe the scaling relation $(\ell_0^{\text{init}} - \ell_0^*) \sim \Delta z$. (b) Atypical negative Poynting effect: Quadratic scaling of the tensile isotropic stress $-p$ with the shear strain γ for $\ell_0 = \ell_0^*$ and $z = 3.2$. (b inset) Prediction of the prefactor in panel b based on the scaling of the critical shear γ^* with $\ell_0 - \ell_0^*$ for $\ell_0 > \ell_0^*$. The black dashed line represents the prediction according to Eq. (S48). (c) Prediction of the prefactor in the linear shear modulus scaling for $\ell_0 < \ell_0^*$ with $\gamma = 0$ based on the scaling of the critical shear γ^* with $\ell_0 - \ell_0^*$ for $\ell_0 > \ell_0^*$. The black dashed line represents the prediction according to the relation $G = 4b(\bar{\ell} - \ell_0)$. (c inset) Prediction of the shear modulus discontinuity ΔG^* for $\ell_0 > \ell_0^*$ based on the scaling of the critical shear γ^* with $\ell_0 - \ell_0^*$. The black dashed line represents the prediction according to Eq. (S41). In panel c and the insets to panels b and c, each symbol represents one probed spring network. In the insets to panels b and c, Z was extracted from the geometric scaling of the respective networks for $\ell_0 < \ell_0^*$, using Eq. (S29).

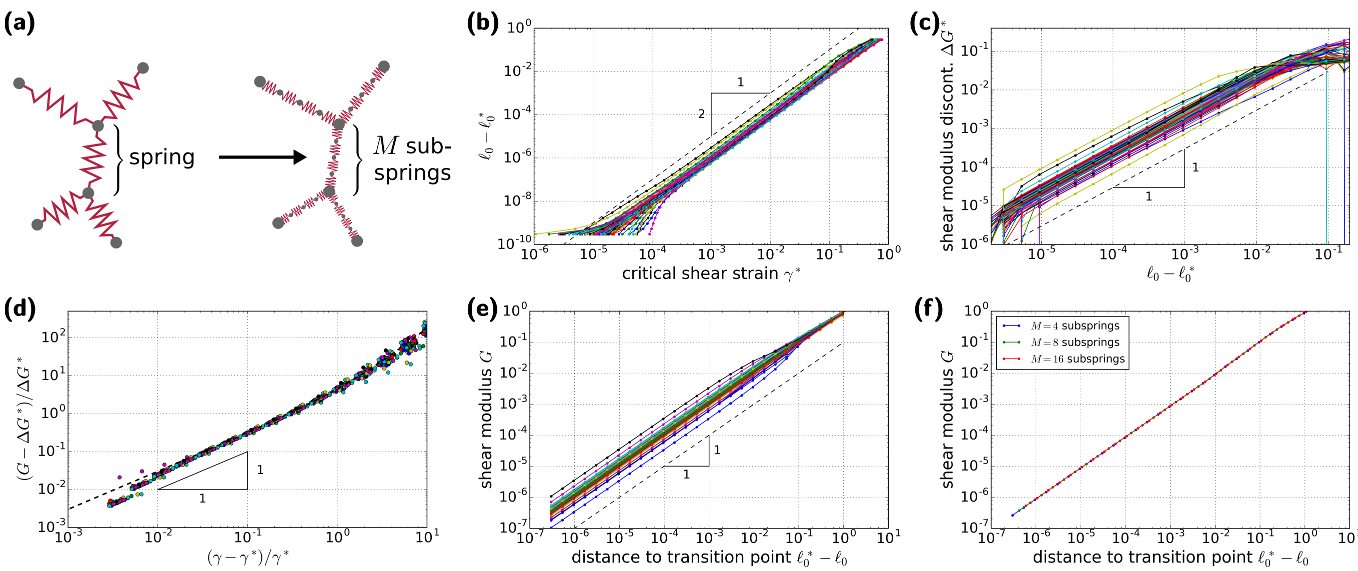

FIG. S6. Our analytical predictions also match fiber network simulations without bending rigidity. (a) To simulate fiber networks, we divide each spring of our original spring networks into M subsprings. We numerically observe (b) a quadratic scaling between critical strain γ^* and $\ell_0^* - \ell_0$ (cf. Fig. 4c in the main text), (c) a linear scaling of the shear modulus discontinuity with $\ell_0^* - \ell_0$ (cf. Fig. 4d inset in the main text), (d) the predicted scaling of the relative excess shear modulus beyond the critical strain γ^* (cf. Fig. 4d in the main text), and (e) a linear scaling of the shear modulus with the mean rest length for $\gamma = 0$ (cf. Fig. 4f in the main text). (f) Simulations with different values for $M > 1$ lead to quantitatively the same predictions, here shown for the plot in panel e for one of the original spring networks. In panels b-e, we set $M = 4$. In panels b-f, we have used for the original spring network a system size of 128 nodes and a connectivity of $z = 3.2$.

tively independent of the number M as long as $M > 1$ (Fig. S6f). This makes sense, because subspring chains under tension will straighten out and thus have the same effect as the original spring, independent of M. Conversely, when replacing springs under compression by a subspring chain, this chain will buckle resulting in a network that behaves as if that subspring chain was not there, independent of $M > 1$. As a consequence of this independence on $M > 1$, the limit $M \to \infty$ is well-defined and corresponds to the behavior of the subspring network with any $M > 1$. Hence, fiber networks without bending rigidity are also faithfully represented by our theory.

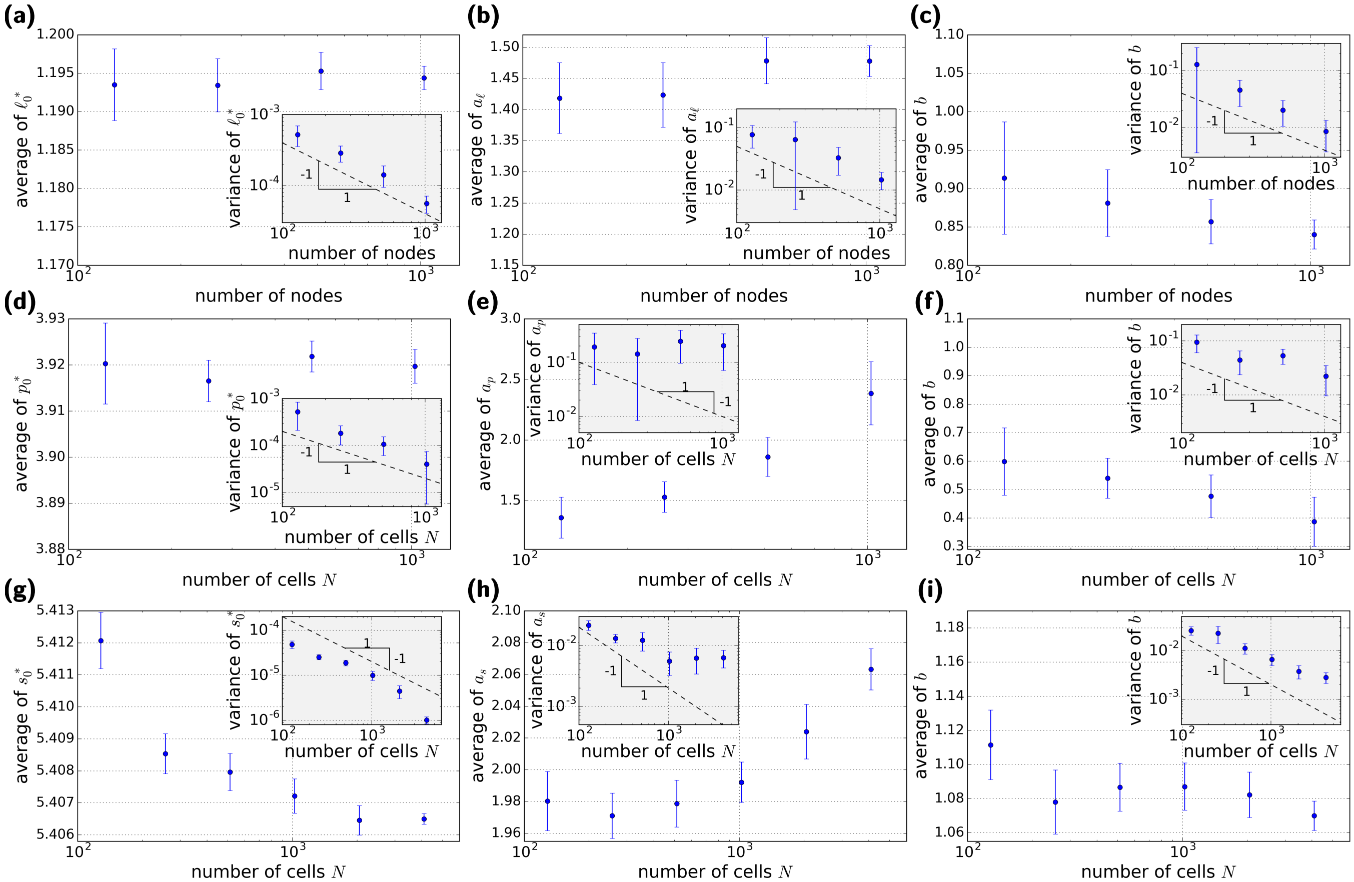

FIG. S7. System-size dependence of the parameters ℓ_0^*, a_ℓ, and b characterizing the $\bar{\ell}_{\min}$ function. (a-c) 2D spring networks with $z = 3.2$, (d-f) 2D vertex model with $k_A > 0$, and (g-i) 3D Voronoi model with $k_V > 0$. For the 2D spring networks, all quantities vary only little with system size. The same is also true for the other models with $k_A = 0$. However, we observe a drift in the a and b coefficients for both models with $k_A > 0$.

D. System-size dependence of the geometric parameters

We also studied the system-size dependence of the parameters ℓ_0^*, a_ℓ, a_a, and b characterizing the $\ell_{\min}$ function. We find that for all models with $k_A = 0$, the parameters do not depend very strongly on system size (e.g. Fig. S7a-c). At the same time their variances decrease with system size as $\sim 1/N$ (Fig. S7 insets).

In contrast, for models with $k_A > 0$, we find a significant, possibly logarithmic, drift in the coefficients a_ℓ, both in two and in three dimensions (Fig. S7e,h). At the same time, the variance in a_ℓ appears to cease decreasing with system size (Fig. S7 insets to e,h). The coefficients b appear to possibly also show such a drift albeit somewhat weaker (Fig. S7f,i & insets). We do not yet know where this drift comes from, but we noted that it is much stronger for the 2D vertex model than for the 3D Voronoi model (Fig. S7e,h).

III. THERE IS AT MOST ONE SELF-STRESS IN THE 2D VERTEX MODEL WITH $k_A = 0$

Here we show analytically that for the $k_A = 0$ case of the 2D vertex model with convex cells, there is at most one self-stress, and that as a consequence the onset of prestresses occurs collectively in *all* cells at once.

For $k_A = 0$, the generalized springs are the N perimeters p_i and the degrees of freedom are the $2N$ vertex positions $\boldsymbol{r}_q$, where q is the vertex index and we assume that all vertices are shared by three cells. Thus, a self-stress in this system is an N-dimensional vector t_i with:

$$\sum_i t_i \frac{\partial p_i}{\partial \boldsymbol{r}_q} = 0 \qquad \text{for all vertices } q. \tag{S62}$$

For a given vertex q, the partial derivative in the sum is only non-vanishing for the three abutting cells (denoted here by i, j, k) such that Eq. (S62) reads for this vertex q:

$$t_i \frac{\partial p_i}{\partial \boldsymbol{r}_q} + t_j \frac{\partial p_j}{\partial \boldsymbol{r}_q} + t_k \frac{\partial p_k}{\partial \boldsymbol{r}_q} = 0. \tag{S63}$$

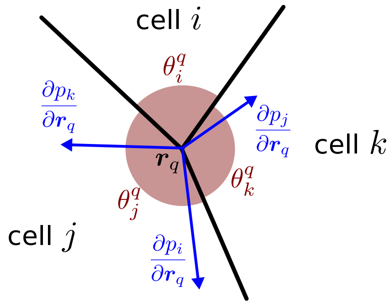

FIG. S8. Definitions of angles for the proof that there is at most one self-stress in the 2D vertex model for $k_A = 0$ (see Section III).

This corresponds to force balance at vertex q with the perimeter tensions t_i, t_j, t_k.

With the angles $\theta_i^q, \theta_j^q, \theta_k^q$ between the cell-cell interfaces (Fig. S8), we obtain for the norm of the perimeter derivatives $|\partial p_i/\partial \boldsymbol{r}_q| = 2\cos(\theta_i^q/2)$, and the direction of $\partial p_i/\partial \boldsymbol{r}_q$ is along the angle bisector of θ_i^q (cf. Fig. S8). If all angles $0 < \theta_i^q < \pi$, then insertion into the force balance equation Eq. (S63) yields

$$\frac{t_i}{\tan(\theta_i^q/2)} = \frac{t_j}{\tan(\theta_j^q/2)} = \frac{t_k}{\tan(\theta_k^q/2)}. \tag{S64}$$

Any solution to Eq. (S62) has to fulfill Eq. (S64) *for each vertex simultaneously*. Thus, in the case where the conditions Eq. (S64) around different vertices are incompatible with each other, there are no nonzero solutions for the t_i. In this case there is no self-stress and thus no prestress, i.e. the system is in the floppy regime. If conversely the conditions Eq. (S64) are compatible with each other for all vertices, a nonzero solution for the t_i exists. However, up to a common factor of proportionality, there is only a single solution, because the factors between the t_i for different cells i are uniquely defined by the relations Eq. (S64). Hence, there is at most only one state of self-stress in this model, and the onset of prestresses occurs in *all* cells at once.

IV. NUMERICAL ENERGY MINIMIZATION

A. Definitions for shear strain γ

For all cellular models, we used as definition for the shear strain γ the simple shear strain (i.e. in the affine case a change in γ corresponds to the displacement $\delta x = y\delta\gamma$ of any point (x, y)). For the 2D spring networks, the shear strain γ denotes pure shear strain defined such that when starting from a quadratic box, the final box aspect ratio is $\exp(\gamma)$. Note that we expect our results to be independent of whether γ denotes simple or pure shear.

B. 2D spring networks

We initialized the spring networks as packing-derived, randomly cut networks as described in the models section in the main text [9, 15]. To improve the precision as compared to the cellular models, we created our own implementation of the Polak-Ribière version of the conjugate gradient minimization method [16], where for the line searches we use a self-developed Newton method based only on energy derivatives. All states were minimized until the average force per degree of freedom was less than 10^{-12}. For the ℓ_0 sweeps (Fig. 1a,b in the main text and Fig. S3a), to prevent switching to a different inherent state, starting from the initial ℓ_0 value we first decreased ℓ_0 in steps of 0.01, each time minimizing the energy. These energy minimizations were shear stabilized with respect to the pure shear degree of freedom (i.e. γ was allowed to vary during energy minimization) [3]. Afterwards, starting again from the initial configuration, we iteratively increased ℓ_0 by steps of 0.01.

For the simulations exploring the vicinity of the $(\gamma, \ell_0) = (0, \ell_0^*)$ point (used for the values in Table I, Figs. 2a, 3a, and 4 in the main text, and Fig. S5), we always first looked for the $(\gamma, \ell_0) = (0, \ell_0^*)$ point using a bisection protocol with pure-shear-stabilized minimizations (see also Section I D). We therefore started with the right (floppy) bracket at the initial ℓ_0 value and the left (rigid) bracket at $\ell_0 = 1.1$, and then executed 25 bisection steps. A configuration was declared rigid whenever the isotropic stress exerted on the boundaries exceeded a value of 10^{-10}.

We explored the rigid vicinity of the transition point $\ell_0 < \ell_0^*$ (used for Figs. 2a, 3a, and 4c inset,f in the main text, and Fig. S5c) starting from $(\gamma, \ell_0) = (0, \ell_0^*)$ by exponentially increasing $\ell_0^* - \ell_0$ starting from a small initial value, and then each time minimizing the energy *without* shear stabilization to ensure $\gamma = 0$ for these simulations. Similarly, we created the γ sweeps for $\ell_0 = \ell_0^*$ (used for Fig. 4e in the main text, and Fig. S5b) by exponentially increasing γ starting from $(\gamma, \ell_0) = (0, \ell_0^*)$ and minimizing without shear stabilization.

We explored the boundary between solid and floppy regime (used for Fig. 4c,d inset in the main text, and Fig. S5c) by exponentially increasing $\ell_0 - \ell_0^*$ starting from $(\gamma, \ell_0) = (0, \ell_0^*)$ without shear stabilization. To reduce the switching to different basins, we chopped large ℓ_0 steps up into smaller steps of 0.01 to include intermittent minimizations. Then, for a given ℓ_0, we increased γ in steps of size 0.001, each time minimizing without shear stabilization. As soon as a rigid state was encountered (isotropic stress on the boundaries exceeds 10^{-10}), we started a bisection starting from the last rigid and the last floppy states encountered as initial brackets. Using 20 bisection steps, we identified γ^*. Once γ^* was identified, we each time scanned 5 different γ values up to 5% above and below γ^* to help us verify that there was indeed a discontinuity in the shear modulus. For Fig. 4d in the main text, we explored the rigid vicinity of the transition more thoroughly using dedicated simulations, where we exponentially increased $\gamma - \gamma^*$ once γ^* for $\ell_0 - \ell_0^* = 10^{-4}$ was identified.

C. 2D vertex model

We always started from Voronoi tessellations of random point patterns, generated using the Computational Geometry Algorithms Library (CGAL, [17]), and we used the BFGS2 implementation of the GNU Scientific Library (GSL, [18]) to minimize the energy. We enforced 3-way vertices and the length cutoff for T1 transitions was set to 10^{-5}, and there is a maximum possible number of T1 transitions on a single cell-cell interface of 10^4. For the p_0 sweeps, we directly minimized the random initial states (used for Figs. 1c,d in the main text, and Figs. S3b, S4a,b). To reduce the number of networks with prestresses in the floppy regime (cf. Fig. S4b), we removed quadrilaterals from the energy-minimized configurations by repeatedly inducing T1 transitions and minimizing the energy until no quadrilaterals were left. Finally, we discarded simulations that had a total force norm larger than 10^{-5}, a shear modulus smaller than -10^{-5}, or a cell-cell interface with length smaller than the T1 cutoff. To explore the solid vicinity of the transition point (used for the values in Table I, Figs. 2b & inset, 3b in the main text, and Fig. S2a), we proceeded using bisection similar to Ref. [2]. First however, we made sure to exclude quadrilaterals from these states. To this end, we first minimized with $p_0 = 3.99$. Then, we repeatedly induced T1 transitions to remove any quadrilaterals followed by another energy minimization until no quadrilaterals were left. This state at $p_0 = 3.99$ was then the right bracket for the bisection and the left bracket was set to 3.8. Then, we proceeded with the bisection as in Ref. [2] with 18 bisection steps and a shear modulus cutoff of 10^{-8}. We excluded configurations were the topology (more precisely, the number of neighbors of all cells) changed between the last rigid and floppy states of the bisection, or during the exploration of the solid vicinity of the transition point. All 2D vertex model configurations studied were shear-stabilized with respect to the simple shear degree of freedom.

D. 2D Voronoi model

We started from random point patterns and minimized the system energy using the BFGS2 routine of the GSL, and we used CGAL to compute the Voronoi tessellations. We discarded simulations that had a total force norm larger than 3×10^{-5}. For the p_0 sweeps, we directly minimized the random initial states (used for Figs. 1c,d in the main text). To explore the solid vicinity of the transition point (used for Table I, Fig. 2b inset in the main text, and Fig. S2a), we proceeded as in Ref. [2] where we started from the initial p_0 bracket $[3.7, 3.9]$ and used 20 bisection steps. The cutoff to declare a configuration as rigid was at a shear modulus of 10^{-6}. To ensure configurations were properly minimized for the exploration of the solid vicinity, we repeated up to 10 minimizations until the force per degree of freedom was smaller than 10^{-8}. We excluded configurations were the topology (the neighbor number of all cells) changed between the last rigid and floppy states of the bisection, or during the exploration of the solid vicinity of the transition point. Due to limitations of the CGAL library, configurations were not shear stabilized.

E. 3D Voronoi model

We used the shear-stabilized energy-minimized states generated in Ref. [2] using the BFGS2 multidimensional minimization routine of the GSL, both regarding the s_0 sweeps (used for Figs. 1e,f in the main text, and Figs. S3c) as well as the simulations exploring the solid vicinity of the transition point (used for Table I, Figs. 2c & inset, 3c in the main text, and Fig. S2c). To explore the solid vicinity of the transition point for $k_V = 0$, we used slightly different numerical parameters. In particular, the initial bracket for the bisection was $[5.34, 5.40]$, and we performed 13 bisection steps, where a state was considered rigid whenever it had a shear modulus greater than 10^{-6}.

[1] T C Lubensky, C L Kane, Xiaoming Mao, A Souslov, and Kai Sun, "Phonons and elasticity in critically coordinated lattices," Reports on Progress in Physics **78**, 73901 (2015), arXiv:1503.01324.

[2] Matthias Merkel and M Lisa Manning, "A geometrically controlled rigidity transition in a model for confluent 3D tissues," New Journal of Physics **20**, 022002 (2018).

[3] Simon Dagois-Bohy, Brian P. Tighe, Johannes Simon, Silke Henkes, and Martin Van Hecke, "Soft-sphere packings at finite pressure but unstable to shear," Physical Review Letters **109**, 1–5 (2012), arXiv:1203.3364.

[4] Dapeng Bi, J. H. Lopez, J. M. Schwarz, and M. Lisa Manning, "A density-independent rigidity transition in biological tissues," Nature Physics **11**, 1074–1079 (2015), arXiv:1409.0593.

[5] Nebojsa Murisic, Vincent Hakim, Ioannis G. Kevrekidis, Stanislav Y. Shvartsman, and Basile Audoly, "From Discrete to Continuum Models of Three-Dimensional Deformations in Epithelial Sheets," Biophysical Journal **109**, 154–163 (2015).

[6] Xingbo Yang, Dapeng Bi, Michael Czajkowski, Matthias Merkel, M. Lisa Manning, and M. Cristina Marchetti, "Correlating Cell Shape and Cellular Stress in

Motile Confluent Tissues," Proceedings of the National Academy of Sciences **114**, 12663–12668 (2017), arXiv:1704.05951.

[7] Daniel Marc Sussman and Matthias Merkel, "No unjamming transition in a Voronoi model of biological tissue," Soft Matter (2018), 10.1039/C7SM02127E, arXiv:1708.03396.

[8] Brian P. Tighe, "Relaxations and rheology near jamming," Physical Review Letters **107**, 1–5 (2011), arXiv:1106.0714v2.

[9] Karsten Baumgarten and Brian P. Tighe, "Normal Stresses, Contraction, and Stiffening in Sheared Elastic Networks," Physical Review Letters **120**, 148004 (2018).

[10] E. Lerner, G. During, and M. Wyart, "A unified framework for non-Brownian suspension flows and soft amorphous solids," Proceedings of the National Academy of Sciences **109**, 4798–4803 (2012), arXiv:1112.0558.

[11] Gustavo Düring, Edan Lerner, and Matthieu Wyart, "Phonon gap and localization lengths in floppy materials," Soft Matter **9**, 146–154 (2013), arXiv:1204.3542.

[12] Karsten Baumgarten, *to be published*, Ph.D. thesis, Delft University of Technology (2018).

[13] A. S. Lodge and J. Meissner, "On the use of instantaneous strains, superposed on shear and elongational flows of polymeric liquids, to test the Gaussian network hypothesis and to estimate the segment concentration and its variation during flow," Rheologica Acta **11**, 351–352 (1972).

[14] Anne S. G. van Oosten, Mahsa Vahabi, Albert J Licup, Abhinav Sharma, Peter A Galie, Fred C. MacKintosh, and Paul A Janmey, "Uncoupling shear and uniaxial elastic moduli of semiflexible biopolymer networks: compression-softening and stretch-stiffening," Scientific Reports **6**, 19270 (2016).

[15] M. Wyart, H. Liang, A. Kabla, and L. Mahadevan, "Elasticity of floppy and stiff random networks," Physical Review Letters **101**, 1–4 (2008), arXiv:0806.4571v1.

[16] Stephen G Nash and Ariela Sofer, *Linear and Nonlinear Programming* (McGraw-Hill College, 1995).

[17] `https://www.cgal.org/`.

[18] `https://gnu.org/software/gsl/`.